Hydro-mechanical processes and their influence on the stimulation effected volume: Observations from a decameter-scale hydraulic stimulation project

Hannes Krietsch[1], Valentin S. Gischig[1,2], Joseph Doetsch[1], Keith F. Evans[1], Linus Villiger[3], Mohammadreza Jalali[4], Benoît Valley[5], Simon Loew[1], Florian Amann[4]

[1]Department of Earth Sciences, ETH Zurich, Zurich, 8092, Switzerland
[2]CSD Ingenieure, Bern, 3097, Switzerland
[3]Swiss Seismological Service, ETH Zurich, Zurich, 8092, Switzerland
[4]Department of Engineering Geology & Hydrogeology, RWTH Aachen, Aachen, 52062, Germany
[5]CHYN, University of Neuchâtel, Neuchâtel, 2000, Switzerland

Correspondence to: Hannes Krietsch (hannes.krietsch@erdw.ethz.ch)

Abstract

Six hydraulic shearing experiments have been conducted in the framework of the In-situ Stimulation and Circulation experiment within a decameter-scale crystalline rock volume at the Grimsel Test Site, Switzerland. During each experiment one out of two different shear zone types were hydraulically reactivated. An extensive monitoring system of sensors recording seismicity, pressure and strain was spatially distributed in eleven boreholes around the injection locations. As a result of the stimulation, the near-wellbore transmissivity increased up to three orders in magnitude, while jacking pressures of the stimulated structures reduced during most of the experiments. Transmissivity change, jacking pressure and seismic activity were different for the two shear zone types, suggesting that the shear zone characteristics govern the seismo-hydro-mechanical response. The elevated fracture-fluid-pressures associated with the stimulations propagated mostly along the stimulated shear zones. The absence of high-pressure signals away from the injection point for most experiments (except two out of six experiments) is interpreted as channelized flow within the shear zones. The observed deformation field within 15 m – 20 m from the injection point is characterized by variable extensional and compressive strain, produced by fracture normal opening and/or slip dislocation, as well as stress redistribution related to these processes. At greater distance from the injection location, strain measurements indicate a volumetric compressive zone, in which the strain magnitude decreases with increasing distance. This compressive strain signals are interpreted as a poro-elastic far-field response to the emplacement of fluid volume around the injection interval. The exceptional hydro-mechanical data reveal that the overall stimulation effected volume is significantly larger than implied by the seismicity cloud, and can be subdivided into a primary stimulated and secondary effected zone.

1 Introduction

The need for CO_2-neutral and nuclear-free energy production has led to global interest in the extraction of deep geothermal energy in Europe. Presently, only a small portion of the worldwide geothermal resources are exploited (Tester et al., 2006). Unfortunately, at the depths where temperatures are high enough for industrial scale electricity production (>150 °C), the natural transmissivities of interconnected fractures in many regions of the world are too small to establish sufficient fluid circulation for effective heat extraction (Manning and Ingebritsen, 1999). Thus, in these regions, the geothermal reservoirs need to be engineered by hydraulic stimulation treatments that aim to sufficiently increase the reservoirs transmissivity (Brown et al., 2012). These engineered heat exchangers, which are mostly located within the crystalline crust, are referred to as engineered/enhanced geothermal systems (EGS) or petrothermal systems. Hydraulic stimulations include two possible endmember mechanism: hydraulic shearing (HS), which denotes the hydraulic reactivation of pre-existing fractures with irreversible shear dilation, and hydraulic fracturing (HF) during which new tensile fractures are initiated and propagated. Both

mechanisms can occur concomitantly under certain conditions that depend upon the in-situ stress field, injection pressure and/or flow rate, initial fracture transmissivity, and fracture network connectivity (McClure and Horne, 2014; Rutledge et al., 2004). HS and HF stimulations involve high-pressure fluid injections into open-hole borehole intervals or through casing perforations, the latter being the norm in the oil and gas industry.

5 Numerous examples of hydraulic stimulation injections in crystalline rocks have shown that they generally give rise to induced seismicity (Evans et al., 2005a; Häring et al., 2008; Parker, 1999; Pearson, 1981; Sasaki, 1998). If the fault slip induced during HS is rapid enough, seismic energy is radiated. Such induced earthquakes can be large enough to be felt at the surface (Davies et al., 2013; Zoback and Harjes, 1997). Thus, one of the main challenges for EGS is: a) keeping the seismic hazard at an acceptable level while b) strongly increasing the reservoirs transmissivity and connectivity. A deeper understanding of the

10 seismo-hydro-mechanical (SHM) responses of rock masses and its fractures to elevated fluid pressure is needed to meet these challenges. Thermoelastic stress perturbations induced by the high temperature differences between rock mass and injection fluid are also important (Tomac and Sauter, 2018), but are not considered in our study which is essentially isothermal.

Quantitative seismological, hydraulic and/or mechanical observations pertaining to reservoir stimulation have been made largely in the context of laboratory experiments (Bandis et al., 1983; Olsson and Barton, 2001; Vogler et al., 2018), and in

15 full-scale field projects (e.g., Basel (Häring et al. 2008) and Soulz-sous-forêt (Evans (2005); Evans et al., (2005b)). Experiments at the intermediate scale are relatively few in number, but are key to bridging the gap in process understanding between these extremes. Several intermediate-scale field projects have been performed to investigate the application of hydraulic stimulation techniques to establish hydraulic linkage between boreholes separated by tens to a hundred meters and at depths of several hundred meters. Examples are the projects at Le Mayet in France (Cornet and Morin, 1997), Falkenberg

20 in Germany (Rummel and Kappelmeyer, 1983), Fjällbacka in Sweden (Wallroth et al., 1999), the Gamma project in Japan (Niitsuma et al, 1989), and Phase 1 of the Rosemanowes project in the UK (MacDonald et al, 1992). In all these projects, the reservoirs were accessed from boreholes drilled from the surface, giving little possibility of installing dense instrumentation in the near-field. Experiments performed at 10-100 m scale within underground rock laboratories, where holes are drilled from galleries, can overcome this limitation. Such experiments generally have a higher degree of complexity than is typical of

25 laboratory scale experiments and thus are more comparable to reservoir stimulations, whilst permitting real-time in-situ monitoring of pressure, deformation, and seismicity occurring in the vicinity of the injection. Amann et al. (2018) identified relevant SHM processes that can be explored in such decameter-scale experiments: a) hydro-mechanical-coupled fluid flow and pressure propagation, b) transient pressure- and permanent slip-dependent permeability changes, c) fracture formation and its interplay with the pre-existing fracture network, d) rock mass deformation around the stimulated fractures due to fault slip

30 and poro-elasticity, e) the transition from aseismic to seismic slip, and f) the spatial and temporal evolution of induced seismicity. To increase the understanding of these processes at the decameter scale, the In-situ Stimulation and Circulation (ISC) project was carried out at the Grimsel Test Site, Switzerland (Amann et al., 2018). A total of six hydraulic shearing and six hydraulic fracturing experiments were conducted within the framework of this project.

In this paper, we focus on the hydro-mechanical-coupled (HM) observations made during the six hydraulic shearing (HS)

35 experiments conducted in February 2016. An overview of the six hydraulic fracturing (HF) experiments that were conducted within the same rock mass in May 2016 is given in Dutler et al. (2019). HF experiments conducted on a smaller scale as part of the stress characterization program are presented by (Gischig et al., 2018; Jalali et al., 2018a; Krietsch et al., 2018c). The analysis of observed induced seismicity is presented by Villiger et al. (2019). An extensive description of the overall project, stimulation experiments, characterization steps, and monitoring setup are presented by Doetsch et al. (2017). Here we seek

40 answer to the following questions:

Q1: How does the transmissivity, induced slip dislocation and injection pressure evolve at the injection interval, and how variable are these outcomes between the experiments?

Q2: How does the transient hydraulic pressure field develop during the stimulation?

Q3: How is the transient and permanent deformation field throughout the volume characterized, and how do adjacent fractures interact in connection with the in-situ stress field?

Q4: What is the extent of the pressurized and stimulation effected volume in relation to the seismicity cloud?

Below, we provide a brief literature review related to the research questions.

1.1 Hydro-mechanical processes near the injection well

Field tests have demonstrated that borehole injectivity can be irreversibly enhanced by several orders of magnitudes during stimulation, due primarily to induced irreversible dislocation of fractures (Bao and Eaton, 2016; Davies et al., 2013; Evans et al., 2005b; Kaieda et al., 2000; Zoback and Harjes, 1997). Flow profile measurements (e.g., spinner and temperature logs) conducted during various stimulation projects in crystalline rock show that the majority of the fluid volume injected during stimulation entered the formation through a small number of natural fractures whose transmissivities were permanently increased by the injections (e.g. Fenton Hill (Brown et al., 2012), Le Mayet de Montagne (Cornet and Morin, 1997), Rosemanowes Phase 2 (Parker, 1999); Soultz-sous-forêt (Evans et al., 2005b), Basel (Evans and Sikaneta, 2013). This observation, together with the patterns of microseismicity induced during the injections, suggests that hydraulic activation of pre-existing fractures in shear is the dominant mechanism during the hydraulic stimulation of fractured borehole intervals, at least away from the well (Cornet and Jones, 1994). Hydraulic fractures have been observed at the injection well following stimulation injections at some sites (e.g. Rosemanowes, Fenton Hill (Breede et al., 2013)), although there is some doubt whether they can be driven to propagate far from the injection well (McClure and Horne, 2014). Such fractures would be expected to intersect natural fractures during propagation, which might be reactivated in shear, leading to increasing leak-off from the hydraulic fracture that will ultimately prevent further extension. Nevertheless, McClure and Horne (2014) note that pressure-limiting behavior, which is a common feature of hydraulic fracturing treatments, is also observed for stimulations that are believed to involve hydraulic shearing. Pressure-limiting behavior is best explained by the lift-off or hydraulic jacking of fracture surfaces when the fluid pressure reaches the level of the normal stress acting across fractures carrying the flow. Fractures that support shear stress under ambient conditions will release that stress through slip as effective normal stress decreases, the release being total when lift-off conditions are attained. Thus pressure-limiting behavior is consistent with permeability enhancement through hydraulic shearing.

The pressure within fractures required for full hydraulic jacking or lift-off provides a measure of the normal stress component acting on the fractures, and, as such, it is a quantity of importance. Hydraulic jacking pressure can be estimated from flow-pressure (Q-P) cross-plots of data from step-rate or step-pressure tests, which also provide estimates of injectivity. Such tests were performed before and after each of the hydraulic shear stimulations at the ISC site to characterize the local changes in media characteristics. Since the interpretation and uncertainties of these tests are important to this paper, we describe them in some detail in section 3.

1.2 Pressure propagation

The hydro-mechanical (HM) properties of faults depend on their geological predisposition (Caine et al., 1996; Faulkner and Rutter, 2001; Guglielmi et al., 2008). Permeability and compliance may vary by several orders of magnitude along and across a fault zone (Achtziger-Zupančič et al., 2016; Faulkner et al., 2010). The patterns of microseismicity induced during reservoir-scale stimulation experiments in crystalline rock suggest that fracture zones and faults serve as the primary pathways for the penetration of enhanced fluid pressure in the reservoir, and that diffusion occurs along tube-shaped features or planes within the reservoir (Evans et al., 2005a; Fehler et al., 1987). Thus, the flow field is complex and does not conform with idealized radial or dipole geometries (Evans et al., 2005a).

An increase in fluid pressure within a fracture may lead to an increase in the mechanical aperture in two different ways: a) a reversible elastic opening governed by the compliance characteristics of the fracture (Zangerl et al. 2008; Evans and Meier,

1995; Rutqvist, 1995), or b) an irreversible opening arising from shear failure and associated dilation (Lee and Cho, 2002; Rahman et al., 2002). An increased aperture will generally result in a higher fracture transmissivity, although the process is strongly non-linear and dependent upon multiple factors such as mean aperture, contact area and the presence of damage particles (Tsang, 1984; Zimmerman and Main, 2004). Importantly, the transmissivity increase will also affect the propagation

5 of pressure along the fracture inasmuch as the diffusion process becomes non-linear, resulting in a steepening of the pressure front (Murphy et al., 2004; Hummel and Müller, 2009). With increasing fracture dilation and non-linearity of diffusion, the propagating pressure front becomes steeper, in principle ultimately becoming a shock front when the two fracture surfaces are separate and the fracture become infinitely compliant (Murphy and Dash, 1985). Thus, at a given distance to an injection point, pressures build up more rapidly once the pressure front arrives than would be the case for linear diffusion.

10 Segall (1989) and Segall and Fitzgerald (1998) described stress changes within and outside of hydrocarbon and geothermal reservoirs that have suffered a decline in fluid pressure through production. The reservoir is considered to be the volume of rock that has suffered pore pressure depletion through diffusion. They show that within the reservoir, the stress changes are the sum of a poro-elastic body-force induced by the direct pore pressure change (given by $\alpha_B \cdot \Delta P_P$ where α_B is Biot's coefficient) and the elastic deformation it produces (itself dependent upon boundary conditions), whereas outside of the

15 reservoir the stress change is due only to the deformation. Following this, in this paper we use the terms "primary stimulated zone" to mean the volume in which fluid pressure changes reflect direct diffusion via a hydraulic connection to the injection location, and "secondary effected zone" to mean the volume where fluid pressure changes are due only to deformation (i.e. induced stress transfer), without a change in fluid content.

1.3 Mechanical rock mass response

20 If a rock mass at large depth is critically stressed (e.g., Townend and Zoback, 2000), then small increases in fracture fluid pressures can induce hydraulic shearing along optimally orientated fractures. In such situations, shear failure can be triggered at large distances from the injection point by relatively small pore pressure increases (Evans et al., 1999; Husen et al., 2007; Saar and Manga, 2003).

Stress transfer and deformation related to fracture slip is often referred to as Coulomb failure stress changes in the literature

25 (Stein, 1999). Slip along a fracture plane leads to formation of compressional and dilatational lobes adjacent to the nodal plane (Fowler, 1990; Zoback, 2010). These slip-induced stress changes are often considered to be a trigger for reactivation of pre-existing fractures outside the pressurized structures, or as a cause of compression of fractures and the host rock (Jung, 2013). Furthermore, induced tensile stresses may induce failure (Hill, 2008), and can lead to the formation of splay (also called wing) cracks. These form usually at an angle of approximately 70° to the plane of the shear fracture (Lehner and Kachanov, 1996).

30 Preisig et al. (2015) have demonstrated that stress interaction between neighboring fractures, due to slip or fracture opening, may affect the pressure propagation and deformation field around the stimulation volume and the stimulation of adjacent fractures zones.

1.4 Extent of the stimulation effected volume

Since direct observations of fracture fluid pressure during the stimulation of full- and intermediate-scale reservoirs are rare

35 owing to the practical difficulties of sensor emplacement, information about pressure propagation usually stems from micro-seismic recordings (e.g., Duboeuf et al., 2017; Evans et al., 2005a; Rutledge et al., 2004) and active seismic velocity tomography (Doetsch et al., 2018; Rivet et al., 2016). However, Duboeuf et al. (2017) argued that induced seismicity is not necessarily directly associated with fluid pressure diffusion, but rather with induced stress perturbations. Thus, the seismic cloud may not necessarily illuminate the zones of highest fracture fluid pressures.

40 Another issue associated with reservoir stimulations concerns the estimation of the volume effected by the stimulation. Seismicity clouds are often used to infer size, shape and growth of the stimulated rock mass (Cipolla and Wallace, 2014;

Mayerhofer et al., 2010; Shapiro et al., 1997). However, there is evidence from some field sites that a significant fraction of the induced slip and deformation was aseismic (Cornet et al., 1998; Duboeuf et al., 2017; Evans et al., 2005a; Guglielmi et al., 2015). Thus, there is some doubt as to the degree to which the seismic cloud represents the rock mass volume that was effected by the hydraulic stimulation treatment.

5 **2 Test site**

The ISC project was conducted at the Grimsel Test Site (GTS), Switzerland. This underground research facility has an overburden of ~480 m and is operated by Nagra (Swiss National Coorperative for the Disposal of Radioactive Waste). The ISC test volume is at the southern end of the laboratory and can be accessed from three tunnels. A total of 15 boreholes were drilled into the test volume for stress measurements (referred to as SBH-boreholes), rock mass characterization, high pressure

10 fluid injection (INJ-boreholes), and monitoring of pressure (PRP-boreholes), strain (FBS-boreholes) and seismicity (GEO-boreholes) (Figure 1).
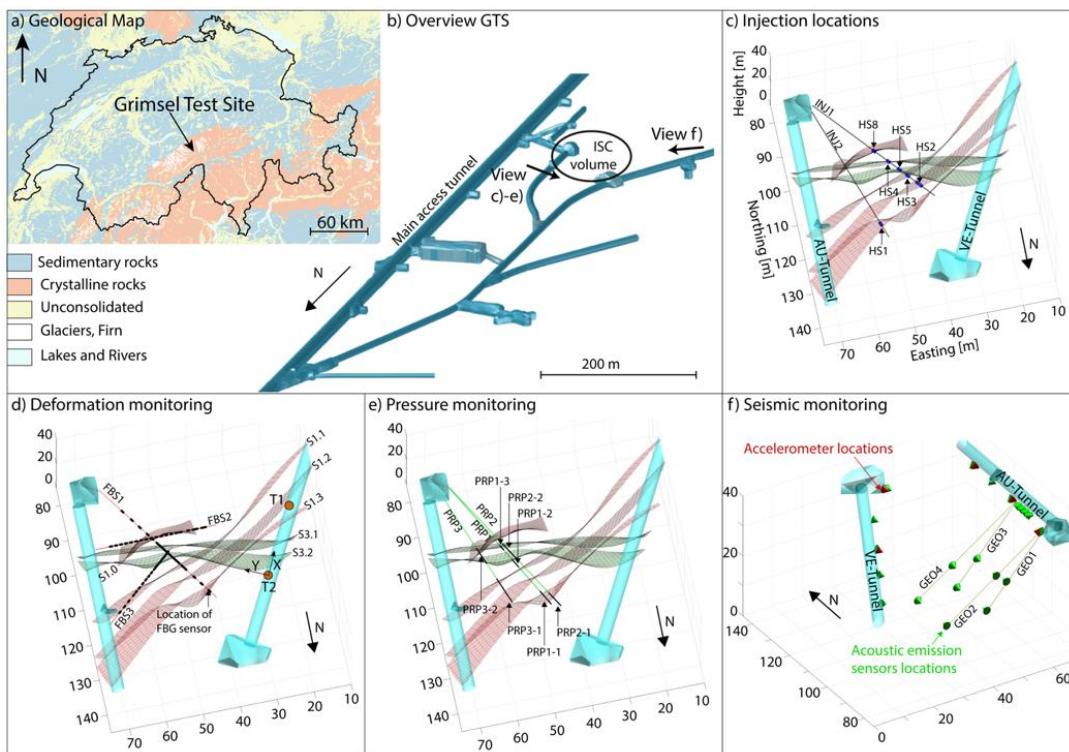
Figure 1. Location of the GTS in Switzerland indicated in the geological map (a), and location of the test volume within the GTS (b). (c) shows the location of the injection intervals together with the target shear zones. d) illustrates locations of the strain sensors and
15 **tilt meters, with indicated tilt axes, and labels the target shear zones. The pressure monitoring intervals are shown in e) and the station locations of the seismic monitoring network is indicated in f).**

2.1 Geology and in-situ state of stress

The GTS is located at the geological boundary between the Grimsel Granodiorite and Central Aar Granite (Keusen et al., 1989). The Early Permian rocks of these lithologies intruded the crystalline crust 299±2 Ma ago (Schaltegger and Corfu, 1992).
20 Both lithologies have a similar quartz content of between 15-30 % (Wenning et al., 2018) and are close to the mineralogical transition between granodioritic and granitic rocks. At the end of the Alpine deformation, the rock mass was exhumed after it

underwent compressional and transpressional deformations at upper greenschist conditions (~450°C and 600 MPa) (Challandes et al., 2008; Goncalves et al., 2012; Wehrens et al., 2016).

In preparation for the stimulation experiments, the geology of the test volume was characterized by performing tunnel mapping and core- and borehole logging (Krietsch et al., 2018b). The rock mass in the test volume contains a pervasive foliation which dips on average towards 140° at an angle of 80°. In addition, the rock mass is intersected by two sets of shear zones (see Figure 1c-f). The older set, referred to as *S1*, contains four subparallel ductile shear zones (Figure 2a) with an average orientation of 142/77 (i.e., dip-direction/dip) (Figure 2c). The shear zones contain few discrete fractures (i.e., brittle discontinuities) inside which formed during low temperature retrograde deformations of the shear zones (Wehrens et al., 2016). Note that the minor *S1* shear zone *HS8* in Figure 2 was not included in the geological model presented by Krietsch et al. (2018b) as it was only recently localized from borehole intersection data and seismicity detected during HS8 (Villiger et al., 2019). The younger set, referred to as *S3*, includes subparallel brittle-ductile shear zones with an average orientation of 183/65 (Figure 2b). Within the test volume, these S3 shear zones coincide with two meta-basic dykes which accommodated most of the brittle-ductile deformation. A total of four *S1* shear zones and two S3 shear zones have been mapped inside the test volume (Krietsch et al., 2018b). Note that the orientations of both shear zone types vary slightly throughout the volume. This is evident in the range of orientations observed at the boreholes that intersect them whose poles are plotted in Figure 2c. The rock mass between the two *S3* shear zones is intensely fractured at the eastern end of the test volume (>20 fractures/borehole meter). Thus, this zone differs from the relatively undisturbed rock mass surrounding these shear zones which has 1-3 fractures per meter.
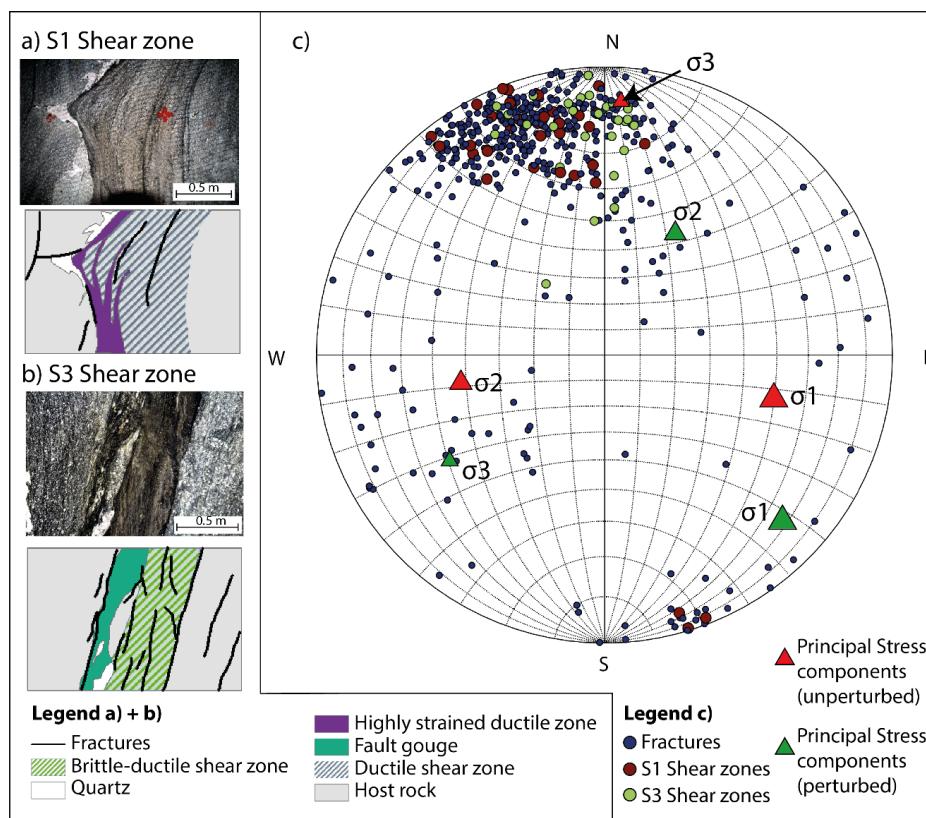
Figure 2. Photographs and interpretations of the *S1* (a) and *S3* (b) shear zones as seen at the tunnel wall (Krietsch et al., 2018b). c) A lower hemisphere stereonet showing the poles of all mapped fractures and shear zones. The orientations of the principal stress components from the unperturbed and perturbed tensor are also shown.

An extensive stress characterization survey was carried out in preparation for the ISC stimulation experiments (Krietsch et al., 2018c). The campaign combined stress relief methods (i.e., overcoring using USBM-probes and CSIRO HI-cells), hydraulic

fracturing, and concomitant seismic monitoring (Gischig et al., 2018; Jalali et al., 2018a). A transverse isotropic elastic rock mass model was required for the inversion of the overcoring data due to the pervasive foliation of the rock mass. A progressive stress field perturbation to an otherwise relatively uniform 'far-field' stress state was observed, that began 11 m from the S3 shear zones, as they were approached from south. The estimated unperturbed principal stress magnitudes were 13.1 MPa (σ_1),

5   9.2 MPa (σ_2) and 8.7 MPa (σ_3). As the shear zone is approached, σ_3 declines to as low at 2.9 MPa immediately before the zone. A CSIRO Hi-cell test conducted at a distance of ~5 m from the shear zone yielded principal stress magnitudes of 13.1 MPa (σ_1), 8.2 MPa (σ_2) and 6.5 MPa (σ_3) and the principal axis orientations that differed from those of the unperturbed tensor, as shown in Figure 2c (Note that this solution is referred to as the perturbed tensor, although the hydraulic fracture and hydraulic jacking tests show that stress was even more strongly perturbed as the shear zone was approached). The origin of the

10 perturbation is unclear, although it may be related to the mechanical property changes associated with the highly fractured zone between the *S3* shear zones at the eastern end of the test volume. For more information on the conducted stress measurements see

The unperturbed stress tensor would imply that the shear stresses acting on the *S1* shear zones tend to be higher than those acting on the S3 shear zones, whereas they are similar for the perturbed stress tensor (Figure 3). Given the necessarily limited

15 spatial coverage of the stress measurements, it is not clear whether the stress perturbation is localized to the shear zone region near the SBH4 borehole, or is representative of the entire shear zone and thus also found at the intersection of the shear zones with the stimulation injection boreholes.
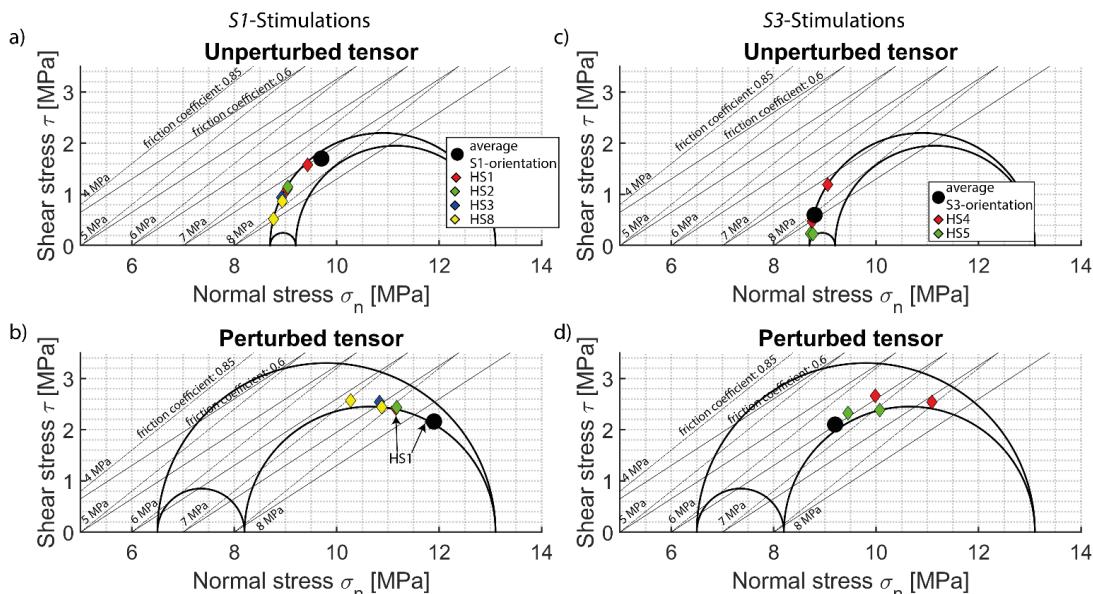
Figure 3. Stress states associated with the perturbed and unperturbed tensors. The implied shear and normal stresses acting on the
20 **S1 and S3 shear zones are indicated. Also shown are the shear and normal stress acting on the principal fractures imaged in the S1**
and S3 stimulation intervals.

3 Methods

The six stimulation experiments targeted four *S1* shear zones and two *S3* shear zones (Table 1 and Figure 1c). Note that during the deformation history of the rock mass, the *S1* shear zones were sheared in a right lateral manner by the *S3* shear zones.

25 Therefore, the *S1* shear zones and the fractures included therein can have a local orientation that is sub-parallel to *S3*. Hence, some of the *S1* shear zone fractures that were injected have an *S3* orientations. The injection intervals for the stimulation experiments were defined on the basis of optical televiewer (OPTV) images and the 3D geological model (Krietsch et al.,

2018b). They had a length of 1 m or 2 m, and covered the target shear zones plus adjacent brittle fractures (**Error! Reference source not found.**). Table 1 summarizes all experiments and geological, hydraulic and mechanical properties of the corresponding injection intervals.

Table 1. Overview stimulation experiment with corresponding information about the injection interval. Note that the experiments are sorted in chronological order.

	Experiment	HS2	HS4	HS5	HS3	HS8	HS1
	Date	08.02.2017	09.02.2017	10.02.2017	13.02.2017	14.02.2017	15.02.2017
	Injection borehole	INJ1	INJ1	INJ1	INJ1	INJ1	INJ2
	Interval depth [m]	38.00-40.00	27.20-28.20	31.20-32.20	34.30-35.30	22.00-23.00	39.75–40.75
Geology	Target shear zone	S1.2	S3.1	S3.2	S1.1	S1.0	S1.3
	Number of brittle fractures	5	>3	>1	2	2	3
Initial interval properties	Interval transmissivity pre-stimulation pulse tests [m²/s]	2.5e-9	1.2e-7	1.2e-8	4.8e-10	2.8e-10	8.3e-11
	Cycle 2 injectivity [lit/min/MPa]	0.018	0.95	0.08	0.0028	0.0019	0.0006
	Cycle 2 jacking pressure [MPa]	4.9	7.1	6.9	4.8	5.4	5.6
Injection	Total volume injected [lit]	797	1253	1211	831	1258	982
	Total Backflow from boreholes [lit]	300.57	109.73	143.63	89.78	175.79	360.995
Final interval properties	Interval transmissivity post-stimulation pulse tests [m²/s]	2.2e-7	1.2e-7	5.5e-8	2.3e-7	7.5e-8	1.5e-7
	Cycle 4 injectivity [lit/min/MPa]	1.62	0.97	0.4	1.69	0.54	1.11
	Cycle 4 jacking pressure [MPa]	4.9	6.8	7.4/8.1	4.7	5.2	3.9

Reactivated Fracture	**Number of reactivated fractures**	1	>2	>2	2	Unclear	1-2
	Cumulative slip dislocation [mm]	0.85 - 1.1	0.6 - 1.6	Unclear	1.1 - 1.4	0.2 - 0.8	0.7 - 0.81

3.1 Injection protocol

We followed the same standardized injection protocol for all six HS experiments to highlight the influence of the target geological structure (i.e., shear zone) on the variability of HM-coupled rock mass responses. The protocol is illustrated in

5   Figure 4 and consisted of four injection cycles, referred to as *C1-C4*, which each consisted of progressively-increased pressure or flow-rate steps. In all cases, the steps were kept constant until steady-state flow conditions were reached. The first two cycles were step-pressure tests, and were intended to estimate the pre-stimulation jacking pressure and injectivity of the target shear zone (see section 3.2). The third cycle was a step-rate test that constituted the actual stimulation phase. The majority of the fluid volume was injected during this cycle, and was intended to propagate the stimulation away from the injection well.

10 The last cycle was performed to estimate the post-stimulation jacking pressure and injectivity (see section 3.2), and began under pressure control but then switched to flow rate control to obtain higher flow rates in the last two injection steps. Each injection cycle was followed by a shut-in phase in which no fluid is injected or released, and a subsequent venting phase. During venting, the pressure line leading to the injection interval was opened to the atmosphere in the AU Tunnel for 20 mins after C1 and C2, and 40 mins after C3. However, the lines leading to the pressure monitoring intervals were opened only for

15 intervals that showed a significant pressure change, and then only after the shut-in phase of C3 and C4. All intervals remained shut-in after C1 and C2. The duration of venting after C3 for those intervals that were opened generally followed the duration of venting of the corresponding injection interval, although the duration was shorter for some intervals in some experiments (e.g. *PRP3.1* in *HS3*). Thus, the induced fluid pressure disturbances within the fractures of the rock mass were partly, but not entirely drained at the beginning of each injection cycle. Following each experiment, all intervals were allowed to drain for 12

20 hours before the next experiment. The total volume of fluid injected in each experiment was limited to approximately 1000 liter to ensure low seismic hazard and little disturbances to nearby experiments (Gischig et al., 2016). The backflows from the injection borehole and all pressure monitoring intervals were measured during the venting phase after each cycle.
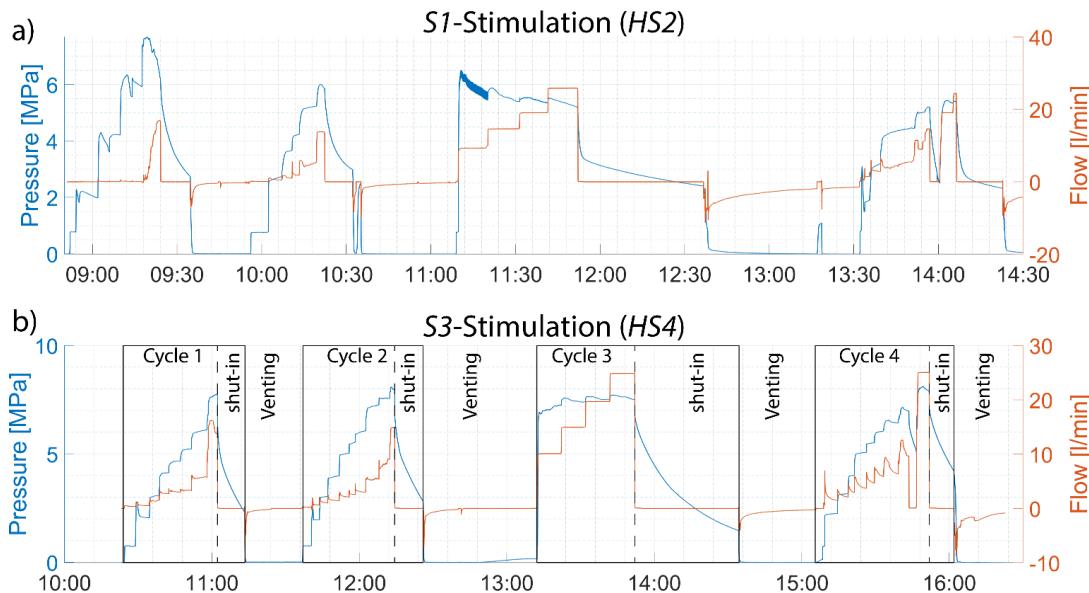
Figure 4. Injection protocol for (a) experiment HS2, which targets S1 structure S1.2, and (b) experiment HS4, which targets S3 structure S3.1. The various phases of the four cycles performed in each experiment are indicated in b. Similar plots for all other intervals are presented in Figure A2 of the Appendix.

5   **3.2 Measurement of hydraulic properties at the injection interval**

To quantify the near-wellbore transmissivity changes of the intervals resulting from the experiments, low-pressure ($P_{injection}$ < 0.5 MPa) hydraulic tests consisting of pulse and constant rate injections were conducted before and after the hydraulic stimulation campaign in each injection interval. The hydraulic properties of the intervals (i.e. transmissivity, storativity, and wellbore storage) were estimated using the numerical simulator nSight[1]. For a more detailed description of the in-situ

10   hydrology and the induced changes, see Jalali et al. (2018a, 2018b).
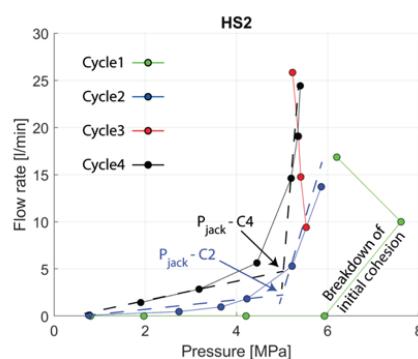
Figure 5. Illustration of the relationship between injection pressure and flow rate during each of the four injection cycles of test HS2. The points denote the P-Q data pairs prevailing at the end of the pressure or flow-rate steps. The slope of the initial linear curve at low pressure for each cycle denotes the interval injectivity. The high pressures reached during the first cycle reflect the breakdown

15   **of the cohesive component of strength and/or initiation of shearing, which are likely to irreversibly increase interval injectivity, as is cycle 3 which is the stimulation. Cycles 2 and 4 are passive intended to work the fracture in the elastic regime so that deviations from the initial linear trend reflect the effect of elastic fracture opening. The jacking pressures for these cycles are taken as the intersection between the low and high-pressure linear trends.**

Hydraulic jacking pressure and injectivity were determined from a Q-P cross-plot of the test data, an example of which is

20   shown in Figure 5. Each point denotes the flow and pressure values at the end of each step when steady-state conditions are

---
[1] An open-source n-dimensional statistical inverse graphical hydraulic test simulator developed by Sandia National Laboratory.

reached, typically after 10 minutes. The first cycle of the test primarily serves to break down the injection interval and so that the fracture changes during subsequent cycles are largely elastic. The low-pressure linear trend on the P-Q plot defines the initial injectivity of the test interval and the intersection with the pressure axis defines the initial formation pressure. In most experiments, the initial injectivity was low and the low-pressure trend was maintained until relatively high pressures were

5   reached before a sudden increase in injectivity denoted breakdown had occurred, as recognized by an increase in flow rate and a decrease in pressure. Breakdown may reflect the breaking of cohesive bonds and perhaps shearing if the fractures support a shear stress (Evans and Meier, 1995). At this point, the injection was stopped and the interval shut-in for 10 minutes before being vented for 20 minutes. The second step-pressure test cycle was then conducted. The low-pressure trend is steeper than in cycle 1, reflecting an increase in injectivity associated with the breakdown. As injection pressure increases, the effective

10   stress on the fractures supporting flow from the interval decreases as pressure diffuses from the injection interval, and the fracture(s), now free of cohesion, will begin to open in accord with their elastic compliance characteristic (Zangerl et al., 2008). The non-linear compliance and the non-linear transformation of opening into injectivity increase, in the simplest case according to the cubic law, gives rise to a progressively steepening P-Q curve which in principle will reach a limiting pressure when the surfaces of the fractures just separate. For a single fracture, the limiting pressure will reflect the normal stress acting on the

15   fracture. This would be the so-called 'jacking pressure'. In practice, the Q-P curve usually transitions to a steep, high-pressure quasi-linear trend rather than a limiting pressure, perhaps reflecting the development of increasing hydraulic losses within or at the entrance to the fractures taking the flow. Dahlø et al. (2003) noted that there is no consensus as to which feature in the Q-P plot provides the best estimation of the jacking pressure (i.e. the normal stress across the fractures that supports the lowest normal stress) because it is unclear at which point along the steepening Q-P curve the compliant fracture response turns into

20   lift-off of the fracture surfaces. Hydropower engineers sometimes pick the first deviation from the low-pressure linear trend as the jacking pressure (eg. Johannesson et al., 1988) as their focus is on the pressure at which hydro-mechanical effects begin to enhance losses from the pressure tunnels, rather than the pressure at which surfaces are just separated, which is of interest here. We take our best estimate of the jacking pressures before and after the stimulation is taken as the intersection of the low- and high-pressure trends of the second and fourth cycles respectively. In both these cycles it is assumed that the response of

25   the fracture network to the step-increases in pressure is purely elastic and repeatable. Shear slip on fractures though which the injected fluid flows could give rise to irreversible increases in aperture with attendant increases of low-pressure transmissivity. However, most shear stress is released in the first cycle which usually extends to significantly higher pressures than subsequent cycles owing to the low injectivity that permanently increases with breakdown.

For the reasons given above, the pre-stimulation jacking pressure and low-pressure injectivity were derived from *C2* of the
30   test data, and the post-stimulation values from *C4* (Figure 7). The injectivity is taken as the ratio between the flow rate and injection pressure at low injection pressures, when mechanical effects are negligible. The jacking pressure was determined during *C2* and *C4* using the method described in section 3.1. In addition, we picked the injection pressure limit during *C3* for all experiments (Figure 7).

3.3 Measurement of slip dislocation at the injection interval

35   Acoustic televiewer (ATV) logs were run before and after each HS experiment. The ATV probe measures the borehole radius with a 360° coverage normal to the borehole axis (Figure 6a). By comparing the geometry of the borehole cross-section across fractures in a borehole it is possible to determine whether dislocation has occurred, and estimate the relative displacement vector (Cornet et al, 1998; Evans et al., 2005b). To enable reasonable comparability between the images, all logs were recentralized using an ellipse fit function. Then, a difference log was produced for each test interval by subtracting the pre-

40   stimulation log from the post-stimulation log. In this difference log, a positive caliper change at a location along the borehole wall indicates that the location has moved away from the borehole axis during stimulation (Figure 6b). The resolved radius changes can be due to: a) stimulation-induced fracture reactivation (i.e., sinusoidal traces along the borehole wall, see Figure

6c (*HS2*)), or b) damage along the borehole wall (i.e., diffuse traces, see Figure 6c (*HS4*)). To validate the orientations and locations of reactivated fractures, the ATV logs were compared with the brittle fractures mapped in the optical televiewer images.
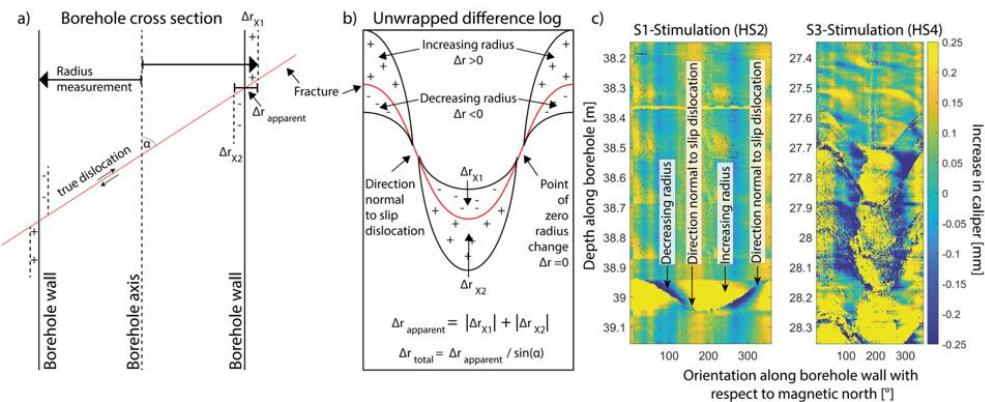
5 **Figure 6. a) Illustration of the travel-time (i.e. radius) measurement of an ATV log across a sheared fracture. b) Observation of slip displacement direction and apparent magnitude estimate visualized in the unwrapped difference log. c) Difference logs for HS2 and HS4 experiments. A clear trace of a reactivated fracture is visible in the HS2 log, whereas a diffuse trace with potential borehole wall damage is shown in the HS4 log.**

To estimate the magnitude of slip dislocation across a reactivated fracture, the areas of radius increase and decrease are mapped

10 along the fracture trace (Figure 6b). The sum of the absolute maximum radius changes on both sides of the fracture (i.e. Δr_{X1} and Δr_{X2}) revealed the apparent amount of slip dislocation ($\Delta r_{apparant}$). Note that the radius changes are measured normal to borehole axis. Thus, the true slip dislocation Δr_{total} is calculated by correcting the apparent dislocation $\Delta r_{apparant}$ by to angle between the borehole axis and the fracture plane (α). The detection threshold for slip dislocation depends on the fracture orientation and ATV accuracy.

15 The direction of the induced slip dislocation can be inferred from the difference logs, too. Along the sinusoidal trace of the reactivated fracture, the radius change varies from positive to negative and back. The location at which these radius change variations occur ($\Delta r = 0$) is normal to the direction of induced permanent dislocation (Figure 6b). Note that this orientation is not well resolved for all experiments.

The ATV probe used for the measurements has a travel time precision of 0.1 µs, yielding a radius precision of 0.07 mm for

20 borehole fluids with a P-wave velocity of 1483 m/s. Note that the travel time precision of the ATV decreases as the measured amplitude of the received P-wave decreases. Thus, the precision strongly decreases as the borehole wall becomes very rough, or the borehole radius becomes strongly elliptical (Moor and Valley, 2018). Since the *S3* shear zones are located in weak meta-basic dykes, which appear rougher at the borehole walls as the *S1* shear zones, the radius resolution is lower for *S3* shear zones than for *S1* shear zones.

25 **3.4 Pressure monitoring**

The three *PRP* boreholes were equipped with a customized grouted packer system that allowed the fluid pressure in several intervals to be continuously monitored during the experiments (Figure 1e). The intervals were chosen to cover the different target shear zone types in the volume, thereby allowing the pressure in these shear zones to be monitored (Table 2). The distances between the monitoring intervals and the injection locations are listed in Table A1. The packer system consists of a

30 grouted section (uppermost part), the open pressure monitoring intervals (2 to 3 per borehole), resin sections in intervals without pressure monitoring and inflatable packers to seal off the monitoring intervals. The packers have a length of 0.2 m and were inflated with pressures between 2 and 3 MPa. The eight intervals were connected to pressure sensors in the AU tunnel

through saturated polyamide lines of 2 mm OD. The sensors used were Keller PAA33-X transmitters that had an accuracy of 0.025 MPa. A detailed description of this packer system can be found in Doetsch et al. (2017).

Table 2. Shear zones sampled by pressure monitoring intervals

Interval name	Depth [m]	Number of fractures	*S1*	*S3*
PRP1-1	41.8 – 47.9	14	S1.2 & S1.3	
PRP1-2	28.9 – 32.0	6		S3.2
PRP1-3	23.2 – 25.2	6		S3.1
PRP2-1	40.0 – 45.0	8	S1.3	
PRP2-2	21.4 – 27.0	11		S3.1 & S3.2
PRP3-1	24.8 – 32.3	4	S1.1 & S1.2	
PRP3-2	15.0 - 20.5	10		S3.1&S3.2

In addition to these fixed pressure monitoring intervals, a double-packer system was installed in the *INJ*-borehole that was not used for injection. The system allowed pressure to be monitored between the two packers, and between the lower packer and borehole bottom. Similarly, the pressure was also monitored between the lower packer and the borehole bottom in the *INJ*-Borehole that was used for injection. The packer systems in the *INJ*-holes were moved for each experiment to allow injection

10 into the shear zone to be stimulated. The pressure monitoring intervals in all boreholes were assigned names formed from the borehole name and the interval number counted from the borehole bottom upwards (e.g. PRP2-1 is the lowermost interval in PRP2).

3.5 Deformation monitoring

3.5.1 Strain monitoring

15 Three boreholes are dedicated to longitudinal strain monitoring (Figure 1d). Borehole *FBS1* intersects all target shear zones, *FBS2* is parallel to the *S3* shear zones, and *FBS3* is subparallel to the *S1* shear zones. 20 Fiber-Bragg-Grating (FBG) strain sensors (Type os3600 by Micron Optics Inc.) were installed in each of these boreholes. The sensors have a base length of 1 m and a resolution of 1 microstrain (με) at a sampling frequency of 1000 Hz. The boreholes were logged with an optical televiewer (OPTV) to provide the information needed to design the system. The optical fiber was then installed in a tube with

20 sensors covering both intact rock mass sections, single and multiple fractures, as well as shear zones (**Error! Reference source not found.**b). Subsequently, the tubes containing the optical fibers were grouted in place.

The sensors were interrogated at 1 kHz, and the data averaged over 1 s intervals before recording, giving a sampling rate of 1 Hz, and an improved resolution of 0.1 με (Krietsch et al., 2018a). Temperature corrections were not applied to the FBG data since the injected fluid had the same temperature as the rock mass and temperature variations within the rock volume were

25 negligible. To quantify deformation, we follow the geomechanics convention and take the compressional strain as positive.

3.5.2 Tilt monitoring

Two horizontal bi-axial inclinometers (Type A711-2 by Jewell Instruments) were installed at the bottom of approximately 50 cm deep boreholes were drilled on the floor of the VE-tunnel (*T1-T2* in Figure 1d). They monitor the deviation from horizontal in two orthogonal axes with an accuracy of ~0.5 microradians (μ-rad) at a sampling rate of 100 Hz. The tilt data were processed

30 with a low pass Butterworth filter with 100 Hz cut-off, which enhances resolution to ~0.05 microradians. The instruments were oriented such that the x-axis was parallel to the tunnel axis and the y-axis normal to it. A positive tilt signal on the x-axis

implies the tunnel floor has dipped towards SWS, and a positive signal on the y-axis implies a dip towards ESE (i.e. towards the test volume) (Figure 1d). Instrument T2 is placed near the intersection of the tunnel with the two S3 shear zones, S3.1 and S3.2, and instrument T1 lies some 13 m to the south, near the intersection of the tunnel with the S1 zones S1.2 and S1.3. The tiltmeters were covered with styrofoam balls to minimize temperature effects.

3.6 Seismic Monitoring

A total of 18 piezo-electric acoustic emission (AE) receivers (Type Ma-Bls-7-70m by GMuG) were installed along the tunnel walls around the test volume. Additionally, eight sensors of the same type were deployed in four dedicated boreholes (i.e., referred to as *GEO* boreholes, Figure 1f). The eight borehole sensors are closest to the injection locations (3 m – 25 m distance) for all six experiments. The sensors have a bandwidth of 1 to 100 kHz. Additionally, five calibrated one-component accelerometers (Type 736T by Wilcoxon) were collocated with the five AE sensors at the tunnel wall for magnitude calibration purposes.

Seismic data were recorded continuously throughout the experiments at a sampling rate of 200 kHz, using a 32-channel acquisition system, with 31 active channels. Induced seismic events were located using an anisotropic velocity model based on manually picked P-wave onsets. For more details on the seismic monitoring and event localization, see Doetsch et al. (2017), Gischig et al. (2018) and Villiger et al. (2019).

4. Results

The multi-faceted monitoring system provides an unusually detailed description of the hydro-mechanical (HM) response during stimulation of the fractures and shear zones contained within the experimental rock volume. As already mentioned, the focus of this contribution is the hydro-mechanical response of the S1 and S3 shear zone types to the stimulation injections, and in particular, to differences between the two (Figure 2). Given the large volume of data recorded, some economies must be made where possible in reporting the results. In the following, we will illustrate the HM observations using the figures for the stimulation experiments *HS2* and *HS4* as examples. Similar observations for all six HS experiments are documented in the appendix. The seismological responses of the rock mass and shear zones are covered in detail by Villiger et al. (2019), and thus only a brief summary will be presented in this paper.

4.1 Hydro-mechanical observations at injection interval

Cross-plots of the pressure and flow rate values prevailing at the end of the steps in the various stages of the six experiments are shown inFigure 6 Figure 7, and the pre-stimulation and post-stimulation jacking pressures, transmissivities and injectivities are listed in Table 1. It is evident that the initial jacking pressures in the two injection intervals covering *S3* shear zones are systematically larger than those for the *S1* shear zones, in most cases by ~1.5 MPa. Following the stimulations, the majority of the intervals showed the same or slightly reduced jacking pressure, with one showing a significant decrease and one a significant increase. The highest drop in jacking pressure of 1.7 MPa was observed for the *S1*-interval *HS1*. The final jacking pressures for the *S1*-intervals varied between 3.9 and 5.5 MPa, whereas for the S3-intervals the variation was 6.8 and 7.4/8.1 MPa. It is also evident that the peak pressures during *C1* for the *S1* stimulations were all much higher than the jacking pressure or pressure limit, suggesting a significant cohesive component to the reopening strength of the zone, whereas no such peak is evident for the *S3* intervals.
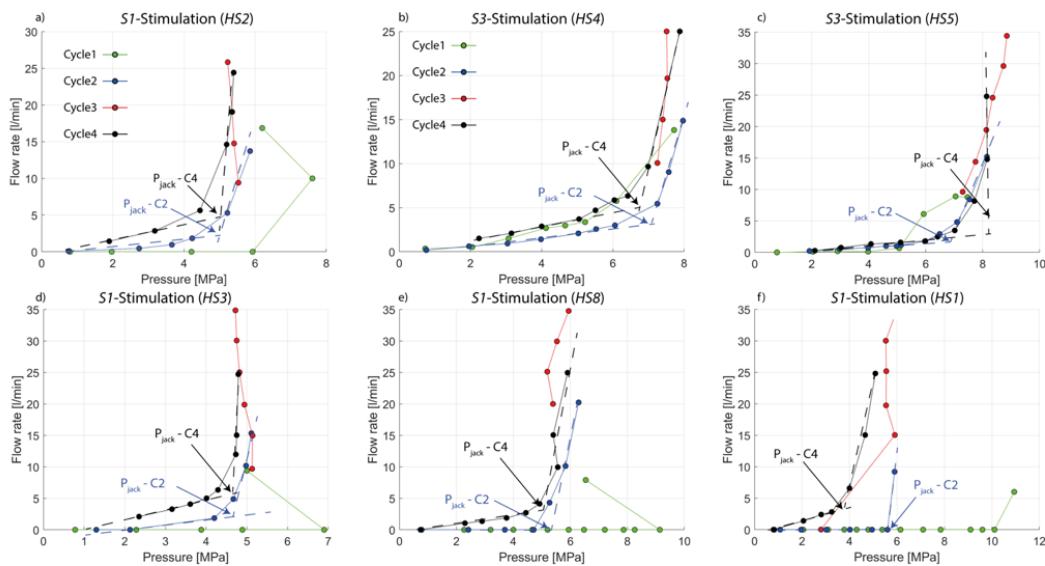
Figure 7. Cross-plots of flow versus pressure data for the four injection cycles of the six stimulation experiments (a-f). The points defining the curves for each cycle denote flow/pressure data pairs defined at the end of each step of the test in question. The first cycle frequently reaches high pressures, which may reflect the inelastic processes of the breakage of cohesive bonds and/or the slippage of fractures supporting shear stress. In subsequent cycles, the response to pressurization is largely elastic and reversible.

Pressure limiting behavior during the stimulation cycle *C3* was observed in all experiments, with some slight systematic differences between the *S1* and *S3* intervals. For the *S3*-stimulations, a slight increase in pressure with increased flow rate was evident, the Q-P curves becoming progressively steeper with increased flow rate as a pressure limit was approached on the final step (Figure 7). In contrast, the *C3* curves for the *S1*-stimulations showed more classic pressure limiting behavior, with pressure monotonically declining with higher flow rate in some cases (i.e. *HS2*, *HS3*), and declining before recovering in others (e.g. *HS1*, *HS8*). The comparison between the injection pressures at the end of the first and last injection steps during *C3* are listed in Table 3. Note, that as for the jacking pressures, the maximum injection pressures attained in the stimulation injections were consistently higher for the *S3* shear zones.

Table 3. Injection pressures measured at the end of the first and last (before shut-in) injection steps of the stimulation injection cycle (*C3*). The difference between the two values is listed in the lower row.

	HS2 (*S1*)	HS4 (*S3*)	HS5 (*S3*)	HS3 (*S1*)	HS8 (*S1*)	HS1 (*S1*)
$P_{Step1\text{-}C3}$ [MPa]	5.53	7.25	7.3	5.13	5.39	5.91
$P_{LastStep\text{-}C3}$ [MPa]	5.23	7.51	8.85	4.72	5.94	5.97
Difference [MPa]	-0.3	+0.26	+1.55	-0.41	+0.55	+0.06

From Table 1 it is clear that initial injectivity and near-well transmissivity for the *S1*-intervals were systematically lower than those for the *S3*-intervals by 1-3 orders of magnitude. Despite this difference, the post-stimulation transmissivities were remarkably similar, all lying within a factor of 2 of 1e07 m^2/s. Thus, substantial transmissivity increases of up to 3 orders of magnitude were realized for the S1 shear zones, whereas the increases for the S3 shear zones were limited to less than an order of magnitude (Figure 8). The final injectivities range between 0.4 – 1.7 l/min/MPa, and the final transmissivities range between 1.2e-7 – 2.3e-7 m^2/s (Table 1).

The measured backflow during the venting of each HS experiment ranged from 9 % (*HS4*) to 37 % (*HS1* and *HS2*) of the injected fluid volume. Since the rock mass was left to drain for only 12 hours between the experiments, the backflow volumes would have been larger had drainage been longer, although not by much as flow rates at the end of the 12 hours were invariably

small. In addition, flow was observed from brittle facture traces at the tunnels during and following the experiments. With the exception of the main flow outlet in the AU tunnel, this flow was not measured during the 12 hour venting.

The estimates of injection-induced slip resolved across fractures in the injection intervals are shown in Figure 8d and the unwrapped difference images shown in Figure A3 of the Appendix. The resolved slip was localized on a single fracture, as in

5 *HS2*, or distributed over various fractures as in *HS4* (Figure 6). The maximum value of ~1.4 mm was found for *HS3*. A value of ~1 mm was obtained for *HS4*, but the uncertainty in this estimate was large because of the greater borehole wall roughness at the *S3* shear zones. The resolution of the ATV data was lower at these zones (*HS4* and *HS5*) (**Error! Reference source not found.**). Dislocations slightly less than a millimeter were also identified for *S1* shear zones *HS1* and *HS2*, and perhaps also *HS8*, although the uncertainty is large. The direction of the slip vector could only be determined for two zones: for *HS2* it was

10 261/02 (i.e., dip direction/dip) and for the two reactivated fractures in *HS3* it was 264/01 and 286/04. All three fractures were reactivated in a right lateral strike-slip dislocation in an east-west direction.
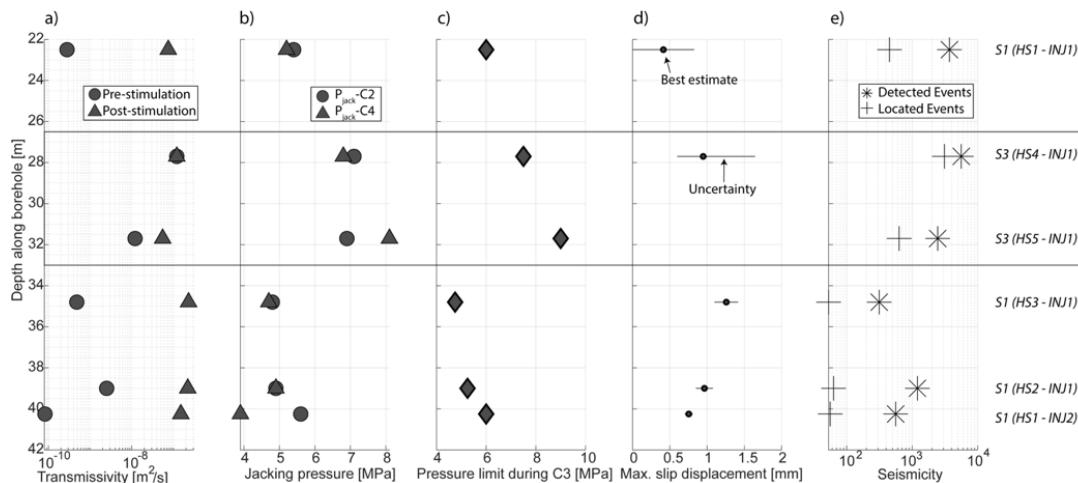
Figure 8. Hydro-mechanical responses of the target intervals to the stimulation experiments. Indicated are (a) pre-and post-stimulation transmissivity, (b) pre- and post-stimulation jacking pressure, (c) injection pressure limit observed during *C3*, (d)
15 **estimated cumulative slip displacement, and (e) number of detected and located seismic events.**

4.2 Hydraulic response

Transient fluid pressure perturbations were observed on almost all *PRP* pressure monitoring intervals during all six hydroshear stimulation experiments. In four experiments, the pressure increases rarely exceeded 1 MPa, regardless of shear zone type,

20 even though peak injection pressures ranged between 5 – 9 MPa (Figure 9 and Figure A4). However, relatively high fluid-pressures were observed during experiments *HS5* and *HS8* (Figure A4). For *HS5*, where injection took place into zone S3.2, the maximum pressure perturbations of 5.7 MPa, 6.7 MPa and 2.7 MPa were observed in *PRP1-2 (S3.2)*, *PRP2-2 (S3.1)* and *INJ2-1 (S1.1, S1.2, and S1.3)* respectively, the latter interval spanning 28.3 - 45.0 m of *INJ2* during this experiment (Table 4). For *HS8*, which featured injection into zone *S1.0*, the maximum perturbation of 4.2 MPa occurred in *INJ2-2,* which spanned

25 depths 5.9 – 18.6 m during *HS8* (Table 4). The *INJ2-2* interval contained only minor fractures, the nearest fracture zone being *S1.0* which intersected *INJ2* 1.5 m from the interval at 20.1 m. Perturbations were also seen in the other pressure monitoring intervals during these two experiments but were minor in comparison. Although one of the monitoring intervals that detected the strong pressure signals covered the target shear zone that was being injected (i.e. *PRP1-2* during *HS5*), the remainder of the strong responses were from intervals that covered other zones, indicating the that shear zones are interconnected. For

30 example, interval *INJ2-1 (S1.1, S1.2 & S1.3)* during *HS5* showed an abrupt rise in pressure to 2.7 MPa towards the end of *C4*

(see Krietsch et al. (under review) for details). However, the majority of intervals outside of the target shear zone registered only minor pressure perturbations.

Table 4. Locations and packed-off length of monitoring intervals in the INJ boreholes during the stimulation experiments. The fracture zones that intersect the interval are given in the adjacent column. Monitoring intervals that include the interval undergoing injection in the other INJ borehole are marked with (*).

Expt. (Zone)	INJ1-1 Depth (m)	Zones	INJ1-2 Depth (m)	Zones	INJ2-1 Depth (m)	Zones	INJ2-2 Depth (m)	Zones
HS2 (S1.2)	41.0 – 45.0	S1.3	38.0 – 40.0 (*)	S1.2	36.2 – 45.0	S1.3	31.5 – 35.2	S1.2
HS4 (S3.1)	29.2 – 45.0	S3.2, S1.1, S1.2, S1.3	27.2 – 28.2 (*)	S3.1	28.3 – 45.0	S1.1, S1.2, S1.3	19.6 – 27.3	S1.0, S3.1, S3.2
HS5 (S3.2)	33.2 – 45.0	S1.1, S1.2, S1.3	31.2 – 32.2 (*)	S3.2	28.3 – 45.0	S1.1, S1.2, S1.3	19.6 – 27.3	S1.0, S3.1, S3.2
HS3 (S1.1)	36.3 – 45.0	S1.2, S1.3	34.3 – 35.3 (*)	S1.1	28.3 – 45.0	S1.1, S1.2, S1.3	19.6 – 27.3	S1.0, S3.1, S3.2
HS8 (S1.0)	24.0 – 45.0	S3.1, S3.2, S1.1, S1.2, S1.3	22.0 – 23.0 (*)	S1.0	19.6 – 45.0	S1.0, S1.1, S1.2, S1.3, S3.1, S3.2	5.9 – 18.6	S1.0, S3.1, S3.2
HS1 (S1.3)	40.7 – 45.0	S1.3	27.0 – 39.7	S1.1, S1.2, S3.1, S3.2	41.75 – 45.	-	39.75 – 40.75 (*)	S1.3

No systematic differences in the recorded pressure magnitude responses to injection into *S1* and *S3* shear zones were evident. However, a tendency for the pressure in the PRP intervals to react more immediately to shut-in after injections into *S1* intervals compared to *S3* intervals can be discerned, particularly at the end of cycle *C3* (Figure 9 and Table A2). This difference is exemplified in Figure 9 where the immediate response of *PRP1-1* (*S1.3*) to *C3* shut-in in *HS2* (injection into zone *S1.2*) can be contrasted with the somewhat delayed reaction of *PRP1-3* and *PRP2-2* (both *S3.1)* to in *HS4* (injection into zone *S3.1*). Indeed, for the *S3*-stimulations, almost all monitoring intervals that included the target shear zone showed a delayed response to the shut-ins.

The pressure in most monitoring intervals at the end of the experiments remained perturbed from their initial values, but in all cases had returned to initial values by the start of the subsequent experiment the following morning (note that the sequence of experimental results in Figure A4 are presented in chronological order). The pressures prevailing in *PRP1-1, PRP2-1,* and *PRP3-1* at the end of the experiments were below the initial values due to the effect of venting the intervals following *C3* and C4 (Figure 9 and Figure A4). It is noteworthy that the venting responses of *S1-3* intervals *PRP1-1* and *PRP2-1*, consistently differed from all other intervals in that significant backflow occurred during venting so that the interval pressure declined relatively slowly. In contrast, the pressure in all other intervals declined rapidly to atmospheric when the value was opened, although it was clear in some cases that backflow into the interval was occurring as the pressure began to climb once the valve was closed (e.g. PRP3-1 (S1.1 and S1.2) in HS4) (Figure 9). Thus, backflow into S1 intervals upon venting tended to be greater that for intervals cutting S3 fracture zones.
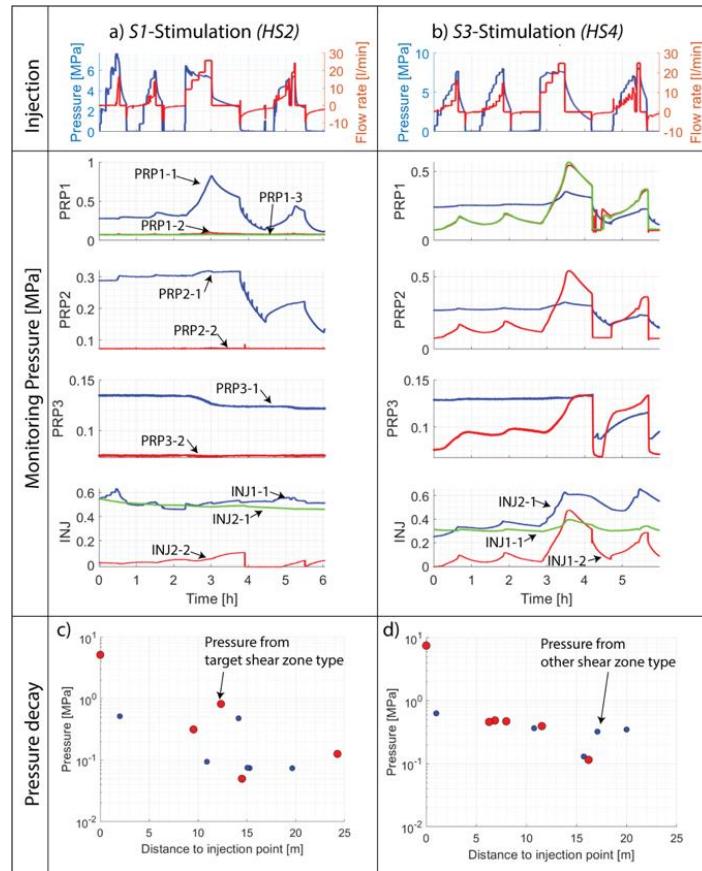
Figure 9. Injection protocols for HS2 and HS4 and the corresponding time series of pressure recorded at the various intervals of the PRP boreholes (a) and b) respectively). The lower frames c) and d) show the pressures prevailing in the intervals at the end of the final step of the C3 injection cycle plotted against the distance to injection point for HS2 and HS4 respectively.

4.2.1 Extent of pressure perturbation

The pressure perturbations from initial levels prevailing at the various monitoring locations at the end of the stimulation injection cycle *C3* are plotted as a function of the straight-line distance from the monitoring intervals to the injection point in Figures 9c/d and 21. These distances, which are listed in Table A1, will generally be less than the true distances of pressure diffusion along hydraulically active fluid pathways. For most stimulations, pressure perturbations were detected out to the furthest monitoring intervals from the target intervals, the largest being 25 m for *PRP1-1* during *HS8* (Figure A5e), although maximum distances during the other stimulations were typically 15-19 m (Figure 9 and Figure A5). No systematic difference in pressure transmission distances for *S1-* and *S3-*stimulations was evident. For both shear zone types, the pressure perturbations registered in intervals that cut the target shear zone tended to be greater than at other intervals located at a comparable distance. There are, however, some exceptions to this. For *HS4,* a relatively weak response was observed at *PRP3-2 (S3.2)* in comparison with other intervals at nearer or comparable distances that did not cover the target shear zone (i.e. *PRP1-3 (S3.2)*, *PRP2-1 (S1.3)*), and *PRP1-1 (S1.3)*.

4.3 Mechanical response

During all HS experiments, the FBG sensors measured compressional and extensional strain perturbations whose magnitudes correlated over time with the injection protocol. Specifically, it was observed that a) the largest strain magnitudes were observed during periods of fluid injection and b) the magnitudes decreased during shut-in and venting. Examples of strain

5 signatures recorded during *HS2* (*S1*) and *HS4* (*S3*) are shown in Figure 10a and b, respectively. For all sensors in all experiments, the strain signatures represent perturbations from the values prevailing at the start of the experiment in question (i.e. zero strain at the start of the experiments). Compressional strains are taken as positive. Since the strain signals denote changes in the relative axial displacement of one end of the baseline with respect to the other divided by the base length, they represent relative axial displacements integrated over the entire FBG base length. As such, they could reflect intact rock

10 deformation and/or fracture dislocation. For each strain signature, we define the permanent (i.e. irreversible) strain as the strain remaining at the end of the experiment, and the reversible strain as the difference between the peak strain and the permanent strain (Figure 10). Here, the peak strain corresponds to the largest strain excursion in the coda, and may be positive (i.e., compressional) or negative (i.e., extensional). In most cases, this peak strain was observed during *C3* (Figure 10a-b), when the largest amount of fluid was injected. Generally, we observe that the reversible strain amplitudes were often larger than the

15 permanent amplitudes, as can be seen from the ratio of the two averaged over all gages for all experiments in Table 5. It is noteworthy that non-zero permanent strains were detected for each experiment on all operation gauges.

Table 5. Ratio between reversible peak strain magnitude (ε_{rp}) and permanent strain magnitude (ε_p), averaged over all operational gauges and all experiments

Experiment	HS2 *(S1)*	HS4 *(S3)*	HS5 *(S3)*	HS3 *(S1)*	HS8 *(S1)*	HS1 *(S1)*
Ratio $\varepsilon_{rp}/\varepsilon_p$	10.1	19.8	222.8	10.0	9.8	4.9

20 ### 4.3.1 Strain along borehole axis

Profiles of strain signals picked at the end of the *C2* and *C3* injections and permanent strains are shown along the three FBG borehole axes in Figure 10 and **Error! Reference source not found.**. Spatial coherence between neighboring gauges is evident along the strain profiles although heterogeneity is also present that in some cases appears to be related to shear zone intersection points. Note that although the boreholes have different orientations, they are not orthogonal. This, together with the

25 heterogeneity of the strain field, precludes the estimation of volume strains from the data.

Within boreholes that are parallel to target shear zones (i.e., *FBS3* for *S1*-stimulations and *FBS2* for *S3*-stimulations), extensional strains were measured at the locations along the borehole axes that lay closest to the injection locations (Figure 10 and **Error! Reference source not found.**). This extension in most cases transitioned into compression within 5 m either up or down the boreholes from this point. In contrast, boreholes that are sub-normal to the target shear zone (i.e., *FBS1* and *FBS2*

30 for *S1*-stimulations, and *FBS1* and *FBS3* for *S3*-stimulation) tended to show compressional strains near the point closest to the injection location (note that this point is not necessarily the borehole intersection of the target shear zone). In a simple way, these tendencies are consistent with expected parallel and normal linear strains along a profile normal to a fracture undergoing an opening-mode dislocation.
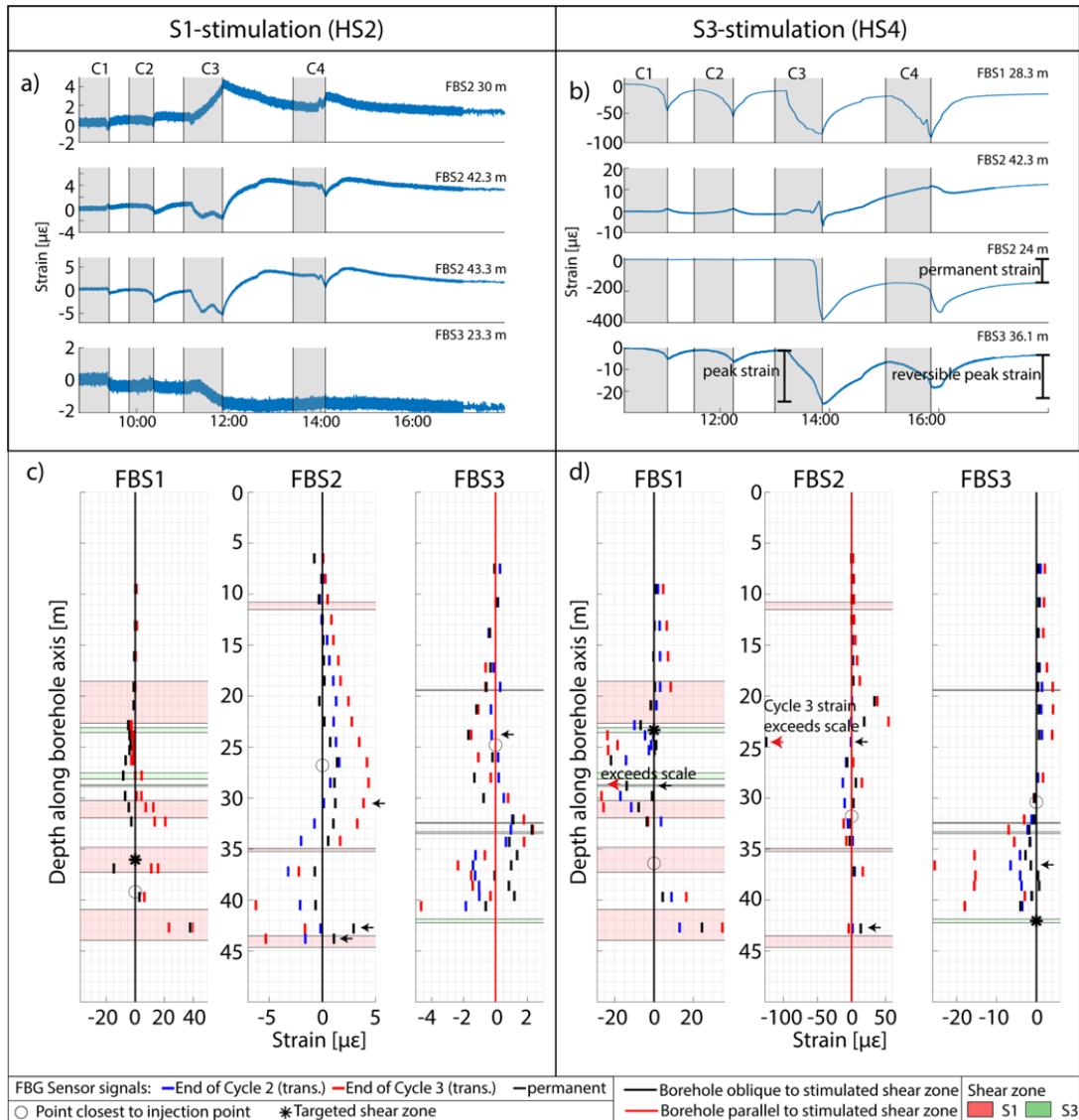
Figure 10. a) and b) Examples of strain time series from four FBGSs during HS2 and HS4 respectively. The vertical shading denotes periods of injection during the four cycles. Examples of the permanent strain, the peak strain and the reversible peak strain are indicated on the HS4 strain codas. c) and d) Profiles of permanent strain, and strain at the end of the injection phases of C2 and C3 along the three FBS boreholes for HS2 and HS4 respectively. The open circle along each borehole denotes the location that lie closest to the injection point for the experiment in question. The pink and green bands indicate places where the holes cut S1 and S3 shear zones respectively. The small black arrows indicate the sensors whose strain codas are shown in a) and b).

4.3.2 Extent of deformation field

Figure 11 and Figure A7 plot the absolute amplitude of the strain signals as a function of distance from the strain gage to the injection point. Tension and compression are distinguished by upward- or downward-oriented triangles respectively. For each experiment, the upper frame shows the strain prevailing at the end of injection in C3, and the lower shows the permanent strain. In most experiments, a general tendency for lower strain amplitudes at greater distance is evident. During almost all experiments, perturbation strain signals larger than 1 με were detected at the FBG furthest away from the injection locations. Thus, the overall extent of the deformed zone was larger than 27-33 m, with respect to radial distance to the injection point.

As noted earlier, points along the boreholes that were close to the injection points showed either extension or compression depending upon whether the borehole and hence the FBG axes were parallel or perpendicular to the target shear zones. Further away from the injection point, the strains in most cases tended to be compressional, regardless of sensor orientation (Figure 11, Figure A7). The transition from this compressional field at distance to a mix of compression and extension (i.e. complex

5 strain field) seemed to occur at slightly larger distances form the injection point for *S1*- than *S3*-stimulations during *C3*. The distances of this transition zone from the injection location are listed in Table 6 for all HS experiments.

Table 6. Distance of strain-transition-zone (change from a variable to compressional strain field) to the injection point, measured at shut-in of injection cycles 2, 3 and 4.

Test name	Shut-in *C2*	Shut-in *C3*	Shut-in *C4*
HS2 *(S1)*	26 m	25 m	23 m
HS4 *(S3)*	16 m	16 m	16 m
HS5 *(S3)*	16 m	12 m	18 m
HS3 *(S1)*	18 m	18 m	18 m
HS8 *(S1)*	16 m	17 m	17 m
HS1 *(S1)*	18 m	18 m	18 m
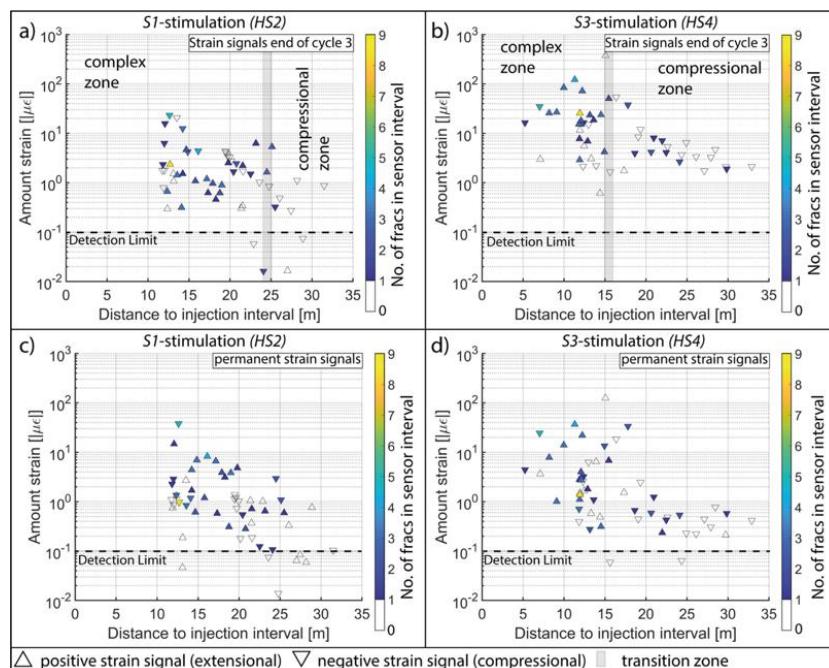
Figure 11. Strain signals with respect to distance to the injection point for HS2 and HS4. Generally, the strain perturbations prevailing at the end of the injection phase of cycle 3 were compressive beyond a certain distance which varied between experiments. This distance is denoted by the vertical grey line in (a) and (b), and separates the compressional zone from the so-called 'complex zone' where a mix of extensile and compressive strains are observed. The color code of the triangle indicates the number of fractures
15 **located within the FBG sensor intervals.**

4.3.3 Tilt measurements

The two inclinometers are located in the floor of the VE tunnel (Figures 1d and 12). Instrument *T2* is located near the intersection of the tunnel with the two *S3* shear zones, *S3.1* and *S3.2*, and instrument *T1* lies some 13 m to the south, near the intersection of the tunnel with the *S1* zones *S1.2* and *S1.3*. The data series presented in Figure 12 and **Error! Reference source**
20 **not found.** show that the floor of the VE-tunnel underwent tilting during all experiments, the magnitudes ranging from -4 to

2 µ-radians (i.e., -23.0e-4° to 11.5e-4°) for both tilt axes. Near-immediate tilt responses were seen to the start and stop of injection in most cycles and most experiments. Figure A8 shows that the largest tilt signals tended to be observed on the instrument closest to the target shear zone. Specifically, for injections into *S1* shear zones, significantly larger signals were seen on instrument *T1*, the sense of the tilt indicating that the tunnel floor tilted away from the target *S1* shear zone towards

5   WNW during the stimulations. Significant permanent tilts remained only after the *HS2* and *HS1* stimulations. During the *S3* stimulation *HS4*, the tunnel floor near *T1* tilted towards east (i.e., towards the test volume), whereas the tunnel floor near *T2*, which lies to the north near the intersection of the *S3* zones with the tunnel, tilted towards west (i.e. away from the test volume). However, the permanent tilts at *T1* and *T2* both indicated tilting towards the east with a similar magnitude. During the other *S3* stimulation *HS5*, *T1* showed tilting to the NW whereas *T2* indicated tilting the SW, with no significant permanent tilt on

10   either instrument. Thus, the transient tilts at both locations indicate similar E-W components of tilting of the tunnel floor away from the test volume, but with opposite north-south components (Figure A8). Note that, in general, the transient tilt signals were often much more pronounced than the permanent signals.
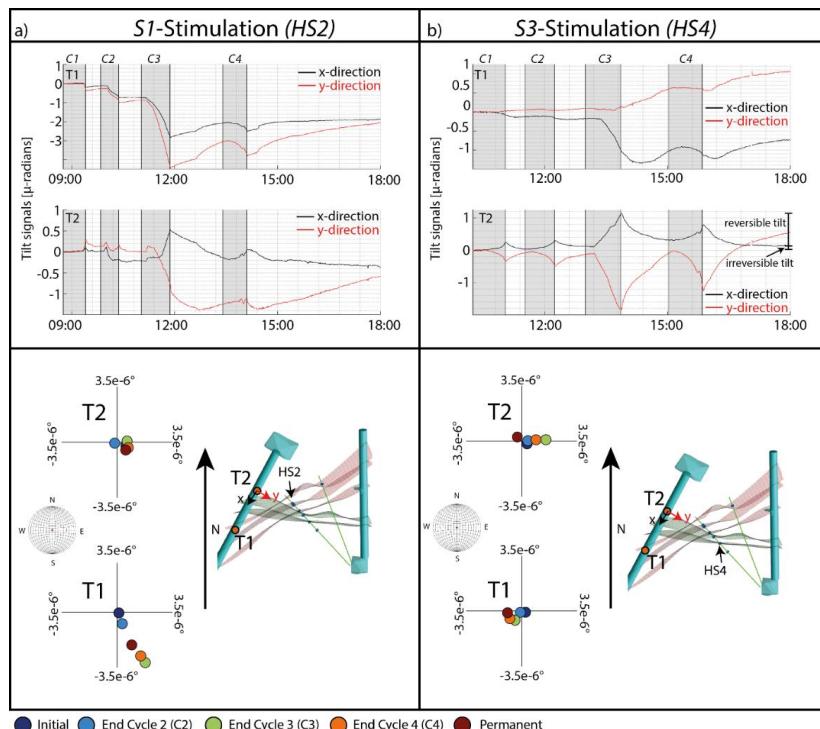
Figure 12. Inclinometer data for a *S1*-stimulation (HS2) (a), and *S3*-stimulation (HS4) (b). The upper panel shows the tilt time series
15   **for both experiments with the injection periods marked by the shaded vertical bands. The lower panel shows a horizontal section through the study volume at the level of the tunnels showing the shear-zones and tiltmeter T1 and T2 positions. The x- and y-axes of the tilt data are indicated on T2. Changes in the downward-oriented normal vector of the tunnel floor at T1 and T2 are shown in the lower-hemisphere plots at the left of the frames.**

4.3.4 Fracture initiation and stress transfer-induced compressional strains

20   During the C3 stimulation phase of experiment *HS4* (injection into *S3.2)* the FBG sensor installed at 24 m depth in *FBS2* indicated strong, very localized extension between the ends of the 1 m baseline of the sensor. No macroscopic fracture was evident on the OPTV images of the interval prior to the experiment. The strain records at 24 m and neighboring sensor locations in *FBS2* are shown in Figure 13 together with the injection protocol for *HS4*. The large extension at 24 m began abruptly near the end of the *C3* injection phase when flow rate was stepped from 20 to 25 l/min, and rapidly developed at rates up to -1.2

25   µε/s to reach a peak strain of ~-370 µε by the end of the injection. Following the experiment, the sensor showed a permanent

strain of -120 µε, implying a reversible peak strain component of -250 µε. The strain responses at this and neighboring sensor locations in *FBS2* to injection during *C1* and *C2* are shown at an expanded scale in the inset of Figure 13. In almost all cases the sensor register extension, although with different magnitudes which range between barely resolved at the 20 m sensor during *C2*, to 8 µε at the 26 m sensor during *C2*. The relatively large strain at the 26 m may be due to the opening of a fracture, which was seen on the OPTV images of the interval. However, all other intervals were free of fractures, and the small strain responses of these intervals to the *C1* and *C2* injections are compatible with a continuum strain field origin for the signals. In contrast, the large extensile strain at 24 m that occurs when the flow rate is stepped from 20 to 25 l/min during *C3* is not consistent with a continuum strain origin. This large extensile strain at 24 m coincides with the development of moderately large compressive strains at 20 and 22 m, and a complex reversal of an initial extensile strain to result in a compressive permanent strain at 26 m. Following injection, all strains progressively decayed to leave a permanent strain. Similar strains responses on the four sensors were observed during the subsequent *C4* injection cycle. We interpret these strain responses as resulting from the opening of a fracture across the 24 m interval that first occurred flow rate was stepped from 20 to 25 l/min during *C3*. This would explain the extension measured at 24 m and compression on the neighboring sensors. Evidently, once opened, the fracture retained a permanent set. Accepting that the 24 m interval contained no fracture prior to the experiment, as suggested by the pre-stimulation OPTV survey, implies that the fracture must have propagated across the interval at the start of the highest-rate phase of the stimulation. Unfortunately, it was not possible to conduct a post-stimulation OPTV survey as the hole was cemented.
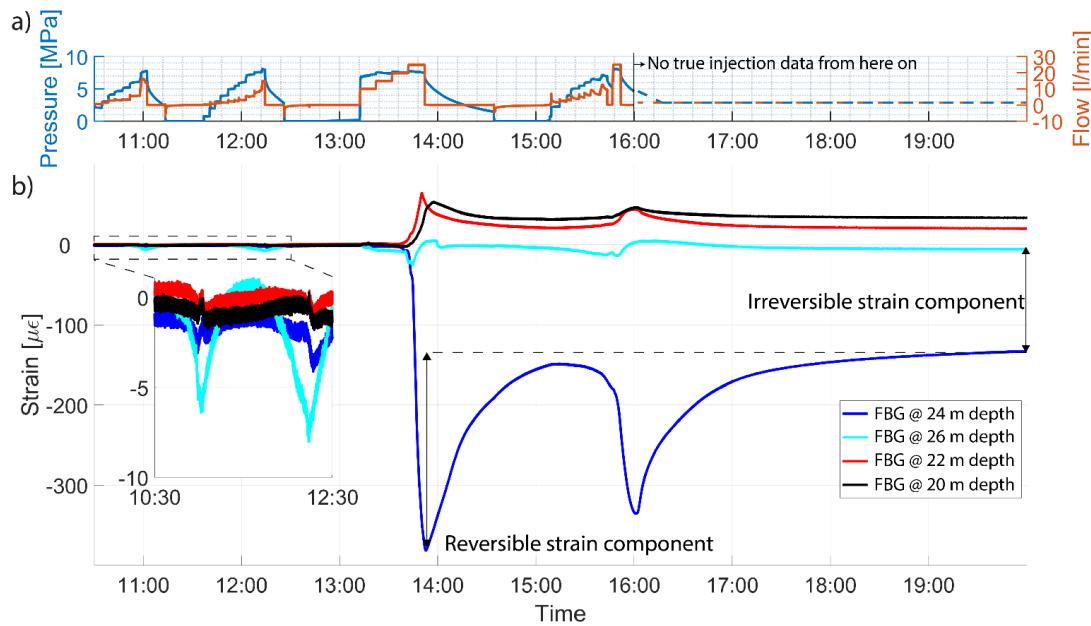
Figure 13. a) injection protocol during the stimulation experiment of interval HS4 with interpolations as dashed line after experiment, b) Strain records at four neighboring FBG sensor locations in FBS2 during HS4. The inset shows the stains at an expanded scale during the first two cycles.

5. Interpretation

Our interpretation is organized in a way that each section seeks answer to one of the research questions (Q1-Q4), mentioned in the introduction.

5.1 Hydro-mechanical processes at the injection interval (Q1)

During the *S1*-stimulations, the peak injection pressures observed during the initial cycle, *C1*, were higher than the jacking pressures derived from *C2* and *C4* or the pressure limit observed during *C3*. This indicates that the pre-existing target fractures had a cohesive component of strength that had to be overcome in order to reopen the fracture. In contrast, this effect was not observed during *S3*-stimulations which suggests that the *S3* shear zones were not so well healed. This fits with the observation that *S3* shear zones had a higher initial transmissivity (Figure 8).

The pre-stimulation transmissivities of the *S1* target structures are 1-2 orders of magnitude lower than those of the two *S3* structures, the *S3.1* zone of *HS4* being the most transmissive at 1.2×10^{-7} m^2/s (Figure 8a). Following stimulation, the transmissivity values of all zones, both *S1* and *S3*, lie with a factor of two of 10^{-7} m^2/s. Thus, the systematically greater increase in the transmissivity of the *S1* zones primarily reflects their lower initial transmissivity. In contrast, the transmissivity of the *S3* interval with the highest initial transmissivity (*HS4*), remained unchanged at 1.2×10^{-7} m^2/s. This may reflect an upper limit on shear-induced irreversible transmissivity enhancement that is linked to the height of asperities along the fracture surface, as inferred at the lab scale by Lee and Cho (2002).

Figure 8 shows that jacking pressures of most intervals remained largely unchanged by the stimulation injections. Exceptions are the *S1*-interval *HS1* (*S1.3*) whose jacking pressure declined from 5.6 MPa to 3.9 MPa, and the *S3*-interval *HS5* whose jacking pressure increased from 6.9 MPa to the range 7.4-8.1 MPa (Table 1). Prior to the stimulations, the jacking pressures of the two *S1* intervals were ~7 MPa, which is systematically higher than the values obtained for the *S1* intervals, which ranged between 4.8 MPa and 5.6 MPa. The origin of this contrast between *S1* and *S3* intervals is uncertain. Jacking pressure is commonly taken as a measure of the stress normal to the fracture plane that is undergoing jacking, and so it is conceivable that the difference reflects the different orientations of *S1* and *S3* structures. However, both the perturbed and unperturbed stress tensors obtained from the stress characterization of Krietsch et al. (2018c) (Figure 3) imply that the *S1* shear zones should have higher normal stresses acting across them than the *S3* shear zones. This inconsistency is best explained as reflecting stress heterogeneity in the stimulated rock volume. The stress characterization of Krietsch et al. (2018c) found that the minimum principal stress dropped from 8 MPa to 3 MPa over an 8 m section of the *SBH4* borehole as an *S3* shear zone was approached. Indeed, the 3 MPa value was a jacking pressure obtained at the margins of the *S3.1* structure. Since this is lower than the jacking pressures obtained across the *S3.1* interval in the *INJ1* borehole, we conclude that stress varies significantly along the structure, and that significant stress heterogeneity is present in the stimulated rock mass.

For all experiments, an injection pressure limit was observed during *C3*. Following Pearson, (1981), we interpret this pressure limit as lift-off of the target shear zone. Evans et al. (2005a) and McClure and Horne, (2014) noted that pressure limiting does not necessarily indicate pure mode I fracture propagation, as it can also occur when shearing occurs (mode II & III), as was observed at several injection points after stimulation. As seen in numerous laboratory experiments (e.g. Esaki et al., 1999; Lee and Cho, 2002), progressive reduction of the effective normal stress across a rough fracture that supports a shear load will eventually lead to slip, which will serve to partly relax the shear stress. This slip will give rise to dilation and damage of the surface, an attendant permeability increase. Continued reduction of effective normal stress can lead to further slip until all shear stress has been relaxed, although the dilation angle for subsequent slip increments generally decreases with net slip. Thus, the amount of dilation and attendant permanent permeability enhancement is limited. Increasing pressures to zero effective normal stress will lead to lift-off of the two sheared surfaces, and pressure-limiting behavior.

The induced slip displacements imaged at the injection intervals occurred along single or multiple fractures. For the *S1* stimulation intervals, one or two fractures tended to be activated, whereas the *S3.1* stimulation interval *HS4* showed evidence to suggest that more than 3 fractures had been reactivated (Figure 6 and **Error! Reference source not found.**). In all cases with multiple reactivated fractures, one fracture trace was dominant in the ATV image. These observations are well in agreement with the observations presented by Evans et al. (2005b) for the Soultz-sous Forêt stimulation projects, respectively.

The direction of the slip induced on each of the planes of interval fractures was compared with the direction of maximum shear stress resolved on the planes using both the unperturbed and perturbed stress tensors. The results listed in Table 7 show that the angle varied between 28° and 45°, depending on which stress tensor was used. Generally, the perturbed stress tensor gave slightly smaller angles than the unperturbed tensor, although the angular misfit is still relatively large. We interpret this to indicate that the perturbed tensor does not adequately represent the degree of local stress field heterogeneity present in the stimulated zone. Generally, the predominant sense of slip observed on the fractures was right lateral strike slip, whereas both tensors predicted a thrusting component for the shear dislocation, which was not observed. Nevertheless, the overall shear sense is similar for the detected dislocations and for the predicted shear stress directions. The angular misfit might also be explained by transient local stress transfer between adjacent fractures during fluid injection at the injection well (Kakurina et al., 2019).

Table 7. Orientation of slip dislocation on the fractures estimated from the pre- and post-stimulation ATV logs, and the maximum shear stresses resolved on the fractures from the unperturbed and perturbed stress tensor. All orientations are given as dip-direction/dip.

		Unperturbed Tensor		Perturbed Tensor	
Experiment	Slip direction	τ_{max}	Misfit [°]	τ_{max}	Misfit [°]
HS2	081/02	081/40	38	077/35	33
HS3	084/01	087/39	41	078/27	28
	106/04		45		30

5.2 Pressure propagation (Q2)

During all HS experiments, the highest fluid pressure perturbations were detected in monitoring intervals that cross the target shear zones. Note that fractures adjacent to the target shear zone also frequently intersect the same pressure monitoring intervals, which renders it impossible to resolve which portion of the pressure signal propagated along the adjacent fracture and within the target shear zone. In contrast, pressure monitoring intervals that do not cover the target shear zone register comparatively minor pressure perturbations of less than 1 MPa during the stimulation experiments. This, indicates that the pressure diffused pre-dominantly along the target shear zones, similar to observations of stimulations at other EGS sites (e.g. at Soultz-sous forêt stimulation experiment (Evans et al., 2005a)).

Murphy et al., (2004) demonstrate that fracture dilation during fluid injection leads to non-linearity of the pressure diffusion field. This gives rise to steeper pressure fronts, which promote more rapid penetration of higher fluid pressures into the rock mass than linear diffusion would imply. In the limit where the fracture faces become separated (i.e. lift-off), the diffusion front appears shock-like. We observed shock-like pressure fronts during two out of the six HS experiments: one for injection into *S1.0* zone during *HS8* and one for *S3.2* shear zone during *HS5*. Aside from these, all other pressure perturbations detected at the monitoring locations were small in comparison, and did not obviously have a form suggestive of non-linear diffusion. The reason for this is uncertain, although it may reflect the limited number of pressure monitoring points in the medium. Evidence of fracture dilation during stimulation was provided by the steepening curves of the Q-P diagrams at higher pressures (Figure 7) and also the FBG strain signals (Figure 10 and **Error! Reference source not found.**) for all HS experiments, and so non-linear diffusion would be expected, at least along target structures. The fact that we observed shock-like pressure fronts only during two experiment might indicate that pressure diffusion was confined to channels within the target shear zone, and these were not sampled by our monitoring intervals. This can be inferred directly from the *HS5* experiment during which a shock-like pressure front appeared first at *PRP2-2* and at a later stage at *PRP1-2*, indicating propagation of the channelized pressure front (Krietsch et al., under review). Thus, we interpret that the non-linear diffusion field propagated along channels through the volume, surrounded by a diffusion field of lower non-linearity or even linear appearance. Two different types of fracture fluid pressure signals were observed during stimulations. The pressure monitoring intervals that cover the target shear zone

often observed a delayed response to shut-in, indicating a diffusion-controlled pressure signal. This type of signal belongs to the primary stimulated zone. On the other hand, pressure intervals that are outside of the target shear zone often responded immediately to shut-in (Figure A4 and Table A2). In some cases, this behavior was detected further away from the injection location than the diffusion-controlled signals. Therefore, we propose that these signals are poro-elastic in nature, and represent

5 the local fracture fluid pressure response to transient far-field stress changes and associated volumetric deformations during stimulation. The different response behaviors are listed in **Error! Reference source not found.**. This poro-elastic far-field effect which occurs outside of the primary stimulated zone within the secondary effected zone has been described by Segall (1989) (see Figure 14).

5.3 Mechanical response and its link to the in-situ stress field (Q3)

10 Strains larger than the 0.1 µε detection limit were observed on all operating FBG sensors during all stimulations, even though some were up to 30 m from the injection points. We observed a transition from a complex strain field to a zone with purely compressional strain that decayed in magnitude with distance. The distance between the transition zone and the injection location at the highest stimulation step (i.e., shut-in of *C3*) ranged between 12 m and 25 m. We interpret the complex strain field as corresponding to the primary stimulated zone. The deformations in this zone reflect stress field changes arising

15 predominantly from effective normal stress reductions across fractures which can produce both normal opening and also relaxation of shear stress through slip (referred to in the literature as Coulomb failure stress change, (Stein, 1999)). The observed magnitude and sign (tension or compression) of these hydro-mechanical deformations strongly depend on the position and orientation of the strain sensor with respect to the stimulated zone. This interpretation is consistent with McClure and Horne (2014) and Rutledge et al. (2004) who note that deformations arising from mode I- and mode II & III-dislocations

20 can occur simultaneously.

The influence of sensor orientation with respect to the target shear zone was highlighted in the complex strain zone, because: a) the majority of sensors oriented sub-normal to the target shear zone detected compressional strains, whereas b) sensors oriented sub-parallel to the target shear zone recorded extensional strains. This effect was predominant for the sensors that spanned only intact rock along their base length. We interpret these observations as reflecting compressive loading of the rock

25 mass adjacent to the plane of the target shear zone by the normal opening of fractures. The extensile strain developed in the orthogonal direction we propose represent a Poisson effect. Taking the ratio of magnitudes of the aforementioned extensional and compression signals, we estimated an average rock mass Poisson's ratio of $\nu_{mean} = \sim 0.33$. Note that other hydro-mechanical responses are superimposed on this Poisson effect in the complex strain field.

Outside this complex strain field, the vast majority of strain measurements show compression, regardless of orientation of the

30 sensors. We interpret this to indicate that the rock mass was compressed as a consequence of the volumetric expansion of the primary stimulated zone The relative absence of extension suggests that the geometry of the primary stimulated zone approximates a *flattened* prolate spheroid: for otherwise extensile strain would occur sub-parallel to the plane of the target structure (Segall, and Fitzgerald, 1998). This secondary effected zone occurred, similarly as for the hydraulic signals, due to the transient far-field stress changes and the coupled volumetric compression (Segall, 1989).

35 While the aforementioned processes were mainly caused by slip and opening of fractures within the primary volume due to effective stress reduction, we also observed potential formation of new fractures that propagated away from the stimulated shear zone (see chapter 4.3.4). These initiated fractures are interpreted as splay cracks, that formed due to tensile stress concentrations induced by shear dislocation along the irregularities (asperities) of the main shear zone (McClure and Horne, 2014). It is also possible that the fractures initiate and locally propagate as mode-1 fractures is local volumes where the

40 minimum principal stress is low due to stress heterogeneity. However, due to significant irreversible strain magnitudes (Figure 13) we argue that the induced dislocation has a dominant mode II/III component.

Based on the sparse tilt data, we were not able to quantify the permanent induced changes within the test volume. Nevertheless, both tiltmeters indicated permanent deformations remained after each of the six experiments, although the reversible components of the tilt magnitudes were larger than the irreversible components (Figure 12 and Figure A8). This can be explained by transient expansion of the primary stimulated zone (Segall and Fitzgerald, 1998). Our data indicate that the poro-elastic far-field responses are at least of similar importance for the description of the transient far-field deformations in the secondary effected zone as the slip-induced stress transfer (i.e. Coulomb failure stress change). Therefore, the poro-elastic response is an important deformation component to consider, but makes deformation field analysis more complex. To analyze the tilt data properly, the source mechanism needs to be modelled which is beyond the scope of this paper.
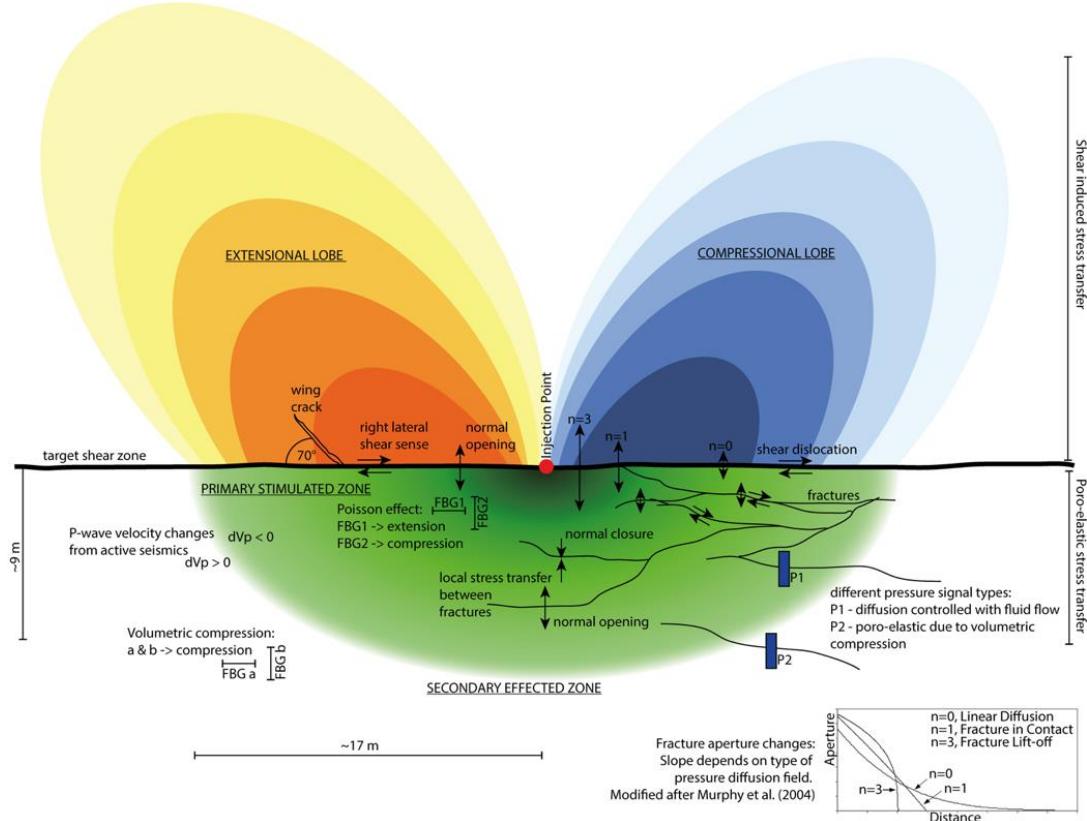
Figure 14. Schematic overview of hydro-mechanical mechanisms active within the 'Primary stimulated zone' about an injection interval. The shape of the Coulomb stress change lobes was modified after Karakostas et al. (2014) and Preisig et al. (2015)).

5.4 Extent of volume effected by the stimulation (Q4)

To estimate the total volume effected by the stimulation during the six stimulation experiments, we combined the observations presented here from the hydraulic (i.e. pressure signals) and mechanical (i.e. strain signals) responses, and integrate the active seismic observations made by Doetsch et al. (2018), Schopper et al. (under review) and passive seismic observations by (Villiger et al., 2019). The pressure monitoring observations indicate that the radial extent of the diffusion-controlled pressure changes extended up to 15 m from the injection point. Beyond this distance, between 15 m and 22 m, the poro-elastic response was dominant. Thus, the transition between the primary stimulated zone and the secondary effected zone was taken as 15 m from injection point. This also corresponds to the transition between the so-called 'complex' strain field, which appeared to be directly effected by active fracture slip and normal opening (Poisson effect), and the compressional strain field, which decayed in magnitude with distance and appeared to be a far-field effect arising from the expansion of the primary stimulated

zone. The extent of the mechanically determined primary stimulation zone depend on the target shear zone properties, such as initial transmissivity and number of reactivated fractures.

Doetsch et al. (2018) and Schopper et al. (under review) used active seismic methods to analyze P-wave velocity changes that were observed during the stimulation experiments. They found that 4D seismic tomograms allowed the tracking of fluid pressure and strain evolution. Close to the injection location, a zone a P-wave velocity decrease was detected that was surrounded by zone of P-wave velocity increase. We propose that the zone of P-wave velocity decrease corresponds to the primary stimulated zone, where deformations are induced by effective normal stress reductions across fractures and slip-induced stress redistributions, and the outer zone of P-wave velocity increase is associated with the secondary effected zone. Here, we consider the isoline marking the 0.1 % of P-wave velocity decrease to denote the boundary between the two stimulated zones (Figure 15). The extent of the isoline was measured parallel and normal to the target shear zone, and was found to be elongated along the target shear zone. This agrees with the observed fluid pressure increases along the shear zone compared to other directions. In general, the P-wave velocity drop reached further from the injection point during *S1*-stimulations than during *S3*-stimulations. This is similar to the observations made for the above described (see Section 4.3.2) transition zone between the different strain fields.
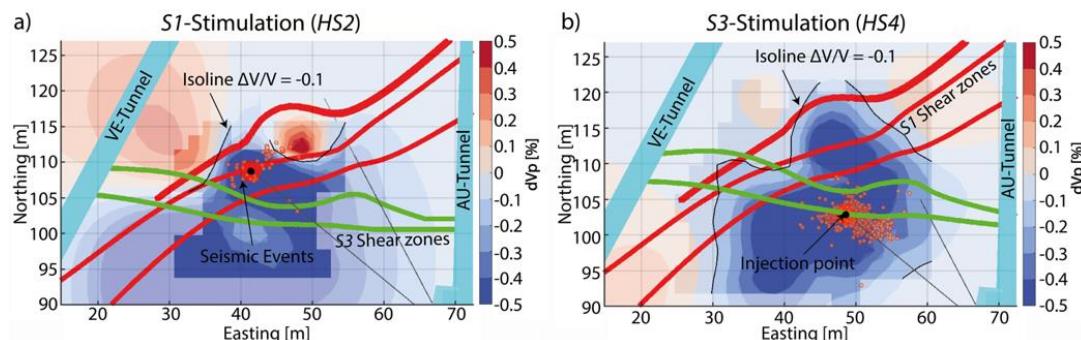
Figure 15. Comparison between active and passive seismic observations during *S1*(a) and *S3*(b) stimulations in map view. The extent of the active seismic velocity change was traced with the -0.1% isoline. This figure was modified after (Schopper et al., under review; Villiger et al., 2019)

Figure 15 also shows located seismic events for the HS2 (S1.2) and HS4 (S3.1) stimulations. The localization accuracy of the seismic events is estimated as ±1.5 m (see Villiger et al. (2019) for details of the microseismic observations). As a general observation, the stimulation of *S1*-zones tended to produce more compact distributions. As was done for the active seismic analysis, we measured the extent of the seismic clouds parallel and normal to the target shear zones. The radial extent of the clouds was found to be similar for both shear zone types and both measured directions (i.e., parallel and normal). However, more seismic events were detected along the target shear zone than normal to it.

Figure 16 summarizes the different radial extents of the stimulation effected volume based on the different measurement methods. The HM observations underline the existence of a primary stimulated and secondary effected zone. The onset of poro-elastic effects in the pressure monitoring data fit the transition from 'complex' strain field to compressional strain field. Note that the poro-elastic effects occur pre-dominantly during *S3*-stimulations. The seismic cloud has a smaller extent than the primary stimulation zone estimates from HM monitoring. Thus, it seems to underestimate the total volume that has been effected by the stimulation. Additionally, Duboeuf et al. (2017) and Guglielmi et al. (2015) stated that a large portion of the stimulation induced dislocation is aseismic. Therefore, we distinguish between the zone that was effected by the stimulation (i.e. including poro-elastic far-field effects) and the zone of stimulation induced permanent dislocations. The active seismics estimated an extent of the primary stimulated zone parallel to the target shear zone that is similar to the HM-based estimations.

Based on the active seismic observations, the primary stimulated zone can be characterized as being ellipsoidal.
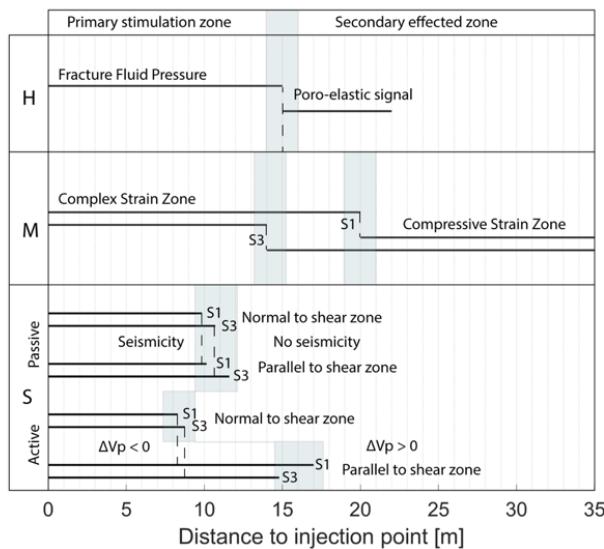
Figure 16. Comparison radial extension stimulated zones determined by hydraulics (H), deformation (M) and seismics (S). For the seismic observations, we distinguish between active seismics (velocity changes) and passive seismics (located seismic events). Note that we did not distinguish between measurement directions for the H and M estimates, as we did not have enough measurement locations to resolve it properly.

6. Conclusions

The six decameter-scale hydraulic shearing experiments conducted at 480 m depth at the Grimsel Test Site, Switzerland have revealed exceptional insights into the hydro-mechanical responses of the crystalline rock mass and fractures to high-rate injections. This was facilitated by a dense array of instrumentation installed in the test volume that included seismometers, pore-pressure- and strain-monitoring boreholes, and inclinometers installed along tunnels. The test volume was cut by two sets of fracture zones, denoted S1 and S3, that had different orientations and different ages. These zones were the target of the stimulation injections. The key results of the experiments can be summarized as follows:

- Systematically lower initial transmissivities by up to 3 orders of magnitude were observed for all four of the intervals that cut S1 target structures, with one S3 interval having a high transmissivity of 10^{-7} m²/s. Following the stimulation, all five other transmissivities were increased to this level. Evidence of shearing was seen on fractures cutting four of the six intervals, but could not be linked to the transmissivity increases as the normal component of dislocation was not estimated.

- Systematically higher initial jacking pressures of ~7 MPa were found for the two S3 intervals, the values for S1 intervals ranging between 4.8 and 5.6 MPa. With one exception, jacking pressures were unchanged by the stimulations. The jacking pressures are low compared to minimum principal stress magnitudes determined in the relatively undisturbed rock mass immediately to the south and almost certainly reflects strong stress heterogeneity in the study volume.

- During the stimulation injections, hydraulic pressure propagated heterogeneously through the target shear zone up to a distance of approximately 15 m distance to injection point. Shock-like pressure fronts observed during two experiments are interpreted as non-linear diffusion along fully-dilated (i.e. wall separation) channels within the target structures. All other pressure perturbations that had delayed arrival times had markedly lower amplitudes, and could have involved linear or non-linear diffusion. Another class of pressure perturbation seen at some measurement points outside the target zone were coincident with changes in injection, and are believed to be poro-elastic in nature.

- All operational FBG strain sensors throughout the study volume detected significant signals during all experiments. Generally, the signals had both transient and permanent strain components, the former being larger than the latter. Strains measured at distances less than 15 m to the injection points were a complex mix of compression and extension, whereas only compression was measured beyond, the magnitude diminishing with distance. The complex near-field zone is believed to correspond to an active zone effected by local stress perturbations arising from normal and shear dislocation of fractures in the target structures, whereas the more distant compression is taken to be the response of the surrounding medium to the volume increase of the active zone and is purely poro-elastic in nature.

- Direct evidence of mode 1 fracture propagation was given by the sudden and pronounced extension of one FBG sensor during a stimulation, with simultaneous compression of neighboring sensors. This is interpreted to reflect the formation of a wing crack from the end of a slip patch on the target structure. Stress communication between different fractures is observed, as strong fracture opening leads to compression of adjacent fractures and the rock mass.

- The dimensions of the microseismic cloud is smaller than the dimensions of the primary stimulated zone as derived from the pressure and strain monitoring systems. The latter is more in accord with the active seismic volume, and is our preferred measure of the stimulated volume.

Acknowledge

This study is part of the In-situ Stimulation and Circulation (ISC) project established by the Swiss Competence Center for Energy Research - Supply of Electricity (SCCER-SoE) with the support of Innosuisse. Funding for the ISC project was provided by the ETH Foundation with grants from Shell and EWZ and by the Swiss Federal Office of Energy through a P&D

20   grant. Hannes Krietsch is supported by SNF grant 200021_169178; Linus Villiger is supported by grant ETH-35 16-1. The Grimsel Test Site is operated by Nagra, the National Cooperative for the Disposal of Radioactive Waste. We are indebted to Nagra for hosting the ISC project in their facility and to the Nagra technical staff for onsite support.

References

Achtziger-Zupančič, P., Loew, S., Hiller, A. and Mariethoz, G.: 3D fluid flow in fault zones of crystalline basement rocks
25   (Poehla-Tellerhaeuser Ore Field, Ore Mountains, Germany), Geofluids, 16(4), 688–710, doi:10.1111/gfl.12192, 2016.

Amann, F., Gischig, V., Evans, K., Doetsch, J., Jalali, M., Valley, B., Krietsch, H., Dutler, N., Villiger, L., Brixel, B., Klepikova, M., Kittilä, A., Madonna, C., Wiemer, S., Saar, M. O., Loew, S., Driesner, T., Maurer, H. and Giardini, D.: The seismo-hydromechanical behavior during deep geothermal reservoir stimulations: open questions tackled in a decameter-scale in situ stimulation experiment, Solid Earth, 9(1), 115–137, doi:10.5194/se-9-115-2018, 2018.

30   Bandis, S. C., Lumsden, A. C. and Barton, N. R.: Fundamentals of Rock Joint Deformation, Int. J. Rock Mech. Min. Sci. & Geomech. Abstr., 20(6), 249–268, 1983.

Bao, X. and Eaton, D. W.: Fault activation by hydraulic fracturing in western Canada, Science, 354(6318), 1406–1409, doi:10.1126/science.aag2583, 2016.

Breede, K., Dzebisashvili, K., Liu, X. and Falcone, G.: A systematic review of enhanced (or engineered) geothermal systems:
35   past, present and future, Geotherm Energy, 1(1), 4, doi:10.1186/2195-9706-1-4, 2013.

Brown, D. W., Duchane, D. V., Heiken, G. and Hriscu, V. T.: Mining the Earth's Heat: Hot Dry Rock Geothermal Energy, Springer Science & Business Media., 2012.

Caine, J. S., Evans, J. P. and Forster, C. B.: Fault zone architecture and permeability structure, Geology, 24(11), 1025, doi:10.1130/0091-7613(1996)024<1025:FZAAPS>2.3.CO;2, 1996.

Challandes, N., Marquer, D. and Villa, I. M.: P-T-t modelling, fluid circulation, and 39Ar-40Ar and Rb-Sr mica ages in the Aar Massif shear zones (Swiss Alps), Swiss Journal of Geosciences, 101(2), 269–288, doi:10.1007/s00015-008-1260-6, 2008.

Cipolla, C. and Wallace, J.: Stimulated Reservoir Volume: A Misapplied Concept?, Society of Petroleum Engineers., 2014.

Cornet, F. H. and Jones, R.: Field Evidences on the Orientation of Forced Water Flow With Respect to the Regional Principal
5 Stress Directions, American Rock Mechanics Association. [online] Available from: https://www.onepetro.org/conference-paper/ARMA-1994-0061 (Accessed 19 December 2019), 1994.

Cornet, F. H. and Morin, R. H.: Evaluation of hydromechanical coupling in a granite rock mass from a high-volume, high-pressure injection experiment: Le Mayet de Montagne, France, International Journal of Rock Mechanics and Mining Sciences, 34(3–4), 207.e1-207.e14, doi:10.1016/S1365-1609(97)00185-8, 1997.

10 Cornet, F. H., Helm, J., Poitrenaud, H. and Etchecopar, A.: Seismic and Aseismic Slips Induced by Large-scale Fluid Injections, in Seismicity Associated with Mines, Reservoirs and Fluid Injections, edited by S. Talebi, pp. 563–583, Birkhäuser Basel., 1998.

Dahlø, T., Evans, K. F., Halvorsen, A. and Myrvang, A.: Adverse effects of pore-pressure drainage on stress measurements performed in deep tunnels: an example from the Lower Kihansi hydroelectric power project, Tanzania, International Journal
15 of Rock Mechanics and Mining Sciences, 40(1), 65–93, doi:10.1016/S1365-1609(02)00114-4, 2003.

Davies, R., Foulger, G., Bindley, A. and Styles, P.: Induced seismicity and hydraulic fracturing for the recovery of hydrocarbons, Marine and Petroleum Geology, 45, 171–185, doi:10.1016/j.marpetgeo.2013.03.016, 2013.

Doetsch, J., Gischig, V., Krietsch, H., Villiger, L., Amann, F., Dutler, N., Jalali, R., Brixel, B., Roques, C., Giertzuch, P., Hochreutener, R., Maurer, H., Wiemer, S., Loew, S., Saar, M., Giardini, D. and Driesner, T.: Grimsel ISC - Experiment
20 Description, Technical Report, ETH Zurich, Zurich, Switzerland., 2017.

Doetsch, J., Gischig, V. S., Villiger, L., Krietsch, H., Nejati, M., Amann, F., Jalali, M., Madonna, C., Maurer, H., Wiemer, S., Driesner, T. and Giardini, D.: Subsurface Fluid Pressure and Rock Deformation Monitoring Using Seismic Velocity Observations, Geophysical Research Letters, 45(19), 10,389-10,397, doi:10.1029/2018GL079009, 2018.

Duboeuf, L., Barros, L. D., Cappa, F., Guglielmi, Y., Deschamps, A. and Seguy, S.: Aseismic Motions Drive a Sparse
25 Seismicity During Fluid Injections Into a Fractured Zone in a Carbonate Reservoir, Journal of Geophysical Research: Solid Earth, 122(10), 8285–8304, doi:10.1002/2017JB014535, 2017.

Dutler, N., Valley, B., Gischig, V., Villiger, L., Krietsch, H., Doetsch, J., Brixel, B., Jalali, M. and Amann, F.: Hydraulic fracture propagation in a heterogeneous stress field in a crystalline rock mass, Solid Earth, 10(6), 1877–1904, doi:10.3929/ethz-b-000379976, 2019.

30 Esaki, T., Du, S., Mitani, Y., Ikusada, K. and Jing, L.: Development of a shear-flow test apparatus and determination of coupled properties for a single rock joint, International Journal of Rock Mechanics and Mining Sciences, 10, 1999.

Evans, K. F.: Permeability creation and damage due to massive fluid injections into granite at 3.5 km at Soultz: 2. Critical stress and fracture strength, Journal of Geophysical Research: Solid Earth, 110(B4), doi:10.1029/2004JB003169, 2005.

Evans, K. F. and Meier, P.: Hydro-jacking and hydrofracturing tests in a fissile schist in south-west Switzerland: In-situ
35 characterization in difficult rock, in Proceedings of the 2nd Int. Conf. on the Mechanics of Jointed and Faulted Rock., 1995.

Evans, K. F. and Sikaneta, S.: Characterisation of natural fractures and stress in the Basel reservoir from wellbore observations (Module 1), in: GEOTHERM – Geothermal Reservoir Processes: Research towards the creation and sustainable use of Enhanced Geothermal Systems, in Swiss Federal Office of Energy Publication, pp. 9–18, Bern, Switzerland., 2013.

Evans, K. F., Hayashi, K., Ito, T., Matsuki, K. and Wallroth, T.: Stress and rock mechanics issues of relevance to HDR/HWR
40 engineered geothermal systems: review of developments during the past 15 years, Geothermics, 28, 455–474, 1999.

Evans, K. F., Moriya, H., Niitsuma, H., Jones, R. H., Phillips, W. S., Genter, A., Sausse, J., Jung, R. and Baria, R.: Microseismicity and permeability enhancement of hydrogeologic structures during massive fluid injections into granite at 3 km depth at the Soultz HDR site: Induced seismicity and flow in deep granite, Geophysical Journal International, 160(1), 389–412, doi:10.1111/j.1365-246X.2004.02474.x, 2005a.

45 Evans, K. F., Genter, A. and Sausse, J.: Permeability creation and damage due to massive fluid injections into granite at 3.5 km at Soultz: 1. Borehole observations, Journal of Geophysical Research: Solid Earth, 110(B4), doi:10.1029/2004JB003168, 2005b.

Faulkner, D. R. and Rutter, E. H.: Can the maintenance of overpressured fluids in large strike-slip fault zones explain their apparent weakness?, Geology, 29(6), 503, doi:10.1130/0091-7613(2001)029<0503:CTMOOF>2.0.CO;2, 2001.

Faulkner, D. R., Jackson, C. A. L., Lunn, R. J., Schlische, R. W., Shipton, Z. K., Wibberley, C. A. J. and Withjack, M. O.: A review of recent developments concerning the structure, mechanics and fluid flow properties of fault zones, Journal of 5 Structural Geology, 32(11), 1557–1575, doi:10.1016/j.jsg.2010.06.009, 2010.

Fehler, M., House, L. and Kaieda, H.: Determining planes along which earthquakes occur: Method and application to earthquakes accompanying hydraulic fracturing, Journal of Geophysical Research: Solid Earth, 92(B9), 9407–9414, doi:10.1029/JB092iB09p09407, 1987.

Fowler, C. M. R.: The Solid Earth, Cambridge Univ. Press, New York, USA., 1990.

10 Gischig, V., Jalali, M., Amann, F., Krietsch, H., Klepikova, M., Esposito, S., Broccardo, M., Obermann, A., Mignan, A., Doetsch, J. and Madonna, C.: Impact of the ISC experiment at the Grimsel Test Site - Assessment of Potential Seismic Hazard and Disturbances, Technical Report, ETH Zurich, Zurich, Switzerland., 2016.

Gischig, V. S., Doetsch, J., Maurer, H., Krietsch, H., Amann, F., Evans, K. F., Nejati, M., Jalali, M. R., Valley, B., Obermann, A. C., Wiemer, S. and Giardini, D.: On the link between stress field and small-scale hydraulic fracture growth in anisotropic 15 rock derived from microseismicity, Solid Earth, 9, 39–61, doi:https://doi.org/10.5194/se-9-39-2018, 2018.

Goncalves, P., Oliot, E., Marquer, D. and Connolly, J. A. D.: Role of chemical processes on shear zone formation: an example form the Grimsel metagranodiorite (Aar massif, Central Alps), Journal of Metamorphic Geology, 30, 703–722, doi:doi:10.1111/j.1525-1314.2012.00991.x, 2012.

Guglielmi, Y., Cappa, F., Rutqvist, J., Tsang, C.-F. and Thoraval, A.: Mesoscale characterization of coupled hydromechanical 20 behavior of a fractured-porous slope in response to free water-surface movement, International Journal of Rock Mechanics and Mining Sciences, 45(6), 862–878, doi:10.1016/j.ijrmms.2007.09.010, 2008.

Guglielmi, Y., Cappa, F., Avouac, J.-P., Henry, P. and Elsworth, D.: Seismicity triggered by fluid injection–induced aseismic slip, Science, 348(6240), 1224–1226, doi:10.1126/science.aab0476, 2015.

Häring, M. O., Schanz, U., Ladner, F. and Dyer, B. C.: Characterisation of the Basel 1 enhanced geothermal system, 25 Geothermics, 37(5), 469–495, doi:10.1016/j.geothermics.2008.06.002, 2008.

Hill, D. P.: Dynamic Stresses, Coulomb Failure, and Remote Triggering, Bulletin of the Seismological Society of America, 98(1), 66–92, doi:10.1785/0120070049, 2008.

Hummel, N. and Müller, T. M.: Microseismic signatures of non-linear pore-fluid pressure diffusion, Geophys J Int, 179(3), 1558–1565, doi:10.1111/j.1365-246X.2009.04373.x, 2009.

30 Husen, S., Bachmann, C. and Giardini, D.: Locally triggered seismicity in the central Swiss Alps following the large rainfall event of August 2005, Geophysical Journal International, 171, 1126–1134, doi:doi: 10.1111/j.1365-246X.2007.03561.x GJI, 2007.

Jalali, M., Gischig, V., Doetsch, J., Näf, R., Krietsch, H., Klepikova, M., Amann, F. and Giardini, D.: Transmissivity Changes and Microseismicity Induced by Small-Scale Hydraulic Fracturing Tests in Crystalline Rock, Geophysical Research Letters, 35 45(5), 2265–2273, doi:10.1002/2017GL076781, 2018a.

Jalali, M. R., Klepikova, M., Doetsch, J., Krietsch, H., Brixel, B., Dutler, N., Gischig, V. and Amann, F.: A Multi-Scale Approach to Identify and Characterize Preferential Flow Paths in a Fractured Crystalline Rock, in 2nd International Discrete Fracture Network Engineering Conference (DFNE), Seattle, USA., 2018b.

Johannesson, P., Schleiss, A. and Korbin, G.: Calaveras project high head pressure tunnel, International water power & dam 40 construction, 40(2), 43–48, 1988.

Jung, R.: EGS — Goodbye or Back to the Future, International Society for Rock Mechanics and Rock Engineering. [online] Available from: https://www.onepetro.org/conference-paper/ISRM-ICHF-2013-022 (Accessed 3 February 2019), 2013.

Kaieda, H., Jones, R. H., Moriya, H., Sasaki, S. and Ushijima, K.: Ogachi HDR reservoir evaluation by AE and geophysical methods, in Proceedings World Geothermal Congress, p. 6, Kyushu - Tohoku, Japan., 2000.

45 Kakurina, M., Valley, B., Guglielmi, Y. and Nussbaum, C.: Slip perturbation during fault reactivation by a fluid injection, Tectonophysics, doi:10.1016/j.tecto.2019.01.017, 2019.

Keusen, H., Ganguin, J., Schuler, P. and Buletti, M.: Felslabor Grimsel: Geology, Technical report 97-14, Nagra and Geotest., 1989.

Krietsch, H., Villiger, L., Doetsch, J., Gischig, V., Evans, K., Brixel, B., Jalali, M., Loew, S. and Giardini, D.: Changing flow paths caused by simultaneous shearing and fracturing observed during hydraulic stimulation, Geophysical Research Letters, 5   under review.

Krietsch, H., Gischig, V. S., Jalali, M. R., Doetsch, J., Valley, B. and Amann, F.: A comparison of FBG and Brillouin strain sensing in the framework of a decameter-scale hydraulic stimulation experiment, in 52nd US Rock Mechanics / Geomechanics Symposium, Seattle, USA., 2018a.

Krietsch, H., Doetsch, J., Dutler, N., Jalali, M. R., Gischig, V., Loew, S. and Amann, F.: Comprehensive geological dataset 10   describing a crystalline rock mass for hydraulic stimulation experiments, Scientific Data, 5, 180269, doi:10.1038/sdata.2018.269, 2018b.

Krietsch, H., Gischig, V., Evans, K., Doetsch, J., Dutler, N., Valley, B. and Amann, F.: Stress Measurements for an In Situ Stimulation Experiment in Crystalline Rock: Integration of Induced Seismicity, Stress Relief and Hydraulic Methods, Rock Mechanics and Rock Engineering, doi:10.1007/s00603-018-1597-8, 2018c.

15   Lee, H. S. and Cho, T. F.: Hydraulic Characteristics of Rough Fractures in Linear flow under normal and shear load, Rock Mechanics and Rock Engineering, 35(4), 299–318, doi:DOI 10.1007/s00603-002-0028-y, 2002.

Lehner, F. and Kachanov, M.: On modelling of 'winged" cracks forming under compression, Int J Fract, 77(4), R69–R75, doi:10.1007/BF00036257, 1996.

MacDonald, P., Stedman, A., and Symons, G.: The UK geothermal hot dry rock R&D programme (No. SGP-TR-141-2). 20   Energy Technology Support Unit, Harwell, Oxfordshire, UK, 1992.

Manning, C. E. and Ingebritsen, S. E.: Permeability of the continental crust: Implications of geothermal data and metamorphic systems, Reviews of Geophysics, 37(1), 127–150, doi:10.1029/1998RG900002, 1999.

Mayerhofer, M. J., Lolon, E., Warpinski, N. R., Cipolla, C. L., Walser, D. W. and Rightmire, C. M.: What Is Stimulated 25   Reservoir Volume?, SPE Production & Operations, 25(01), 89–98, doi:10.2118/119890-PA, 2010.

McClure, M. W. and Horne, R. N.: An investigation of stimulation mechanisms in Enhanced Geothermal Systems, International Journal of Rock Mechanics and Mining Sciences, 72, 242–260, doi:10.1016/j.ijrmms.2014.07.011, 2014.

Moor, L. and Valley, B.: Test de la fidélité des données acquises avec un televiewer acoustique pour l'étude de la stabilité des puits géothermiques profonds, unpublished report, CHYN, University of Neuchâtel, Neuchâtel, Switzerland., 2018.

30   Murphy, H. and Dash, Z.: Shocking behavior of fluid flow in deformable joints, Los Alamos National Lab., NM (USA). [online] Available from: https://www.osti.gov/biblio/5626367 (Accessed 19 December 2019), 1985.

Murphy, H., Huang, C., Dash, Z., Zyvoloski, G. and White, A.: Semianalytical solutions for fluid flow in rock joints with pressure-dependent openings, Water Resources Research, 40(12), doi:10.1029/2004WR003005, 2004.

Niitsuma, H. "Fracture mechanics design and development of HDR reservoirs—concept and results of the Γ-Project, Tohoku 35   University, Japan." *International Journal of Rock Mechanics and Mining Sciences & Geomechanics Abstracts*. Vol. 26. No. 3-4. Pergamon, 1989.

Olsson, R. and Barton, N.: An improved model for hydromechanical coupling during shearing of rock joints, International Journal of Rock Mechanics and Mining Sciences, 38(3), 317–329, doi:10.1016/S1365-1609(00)00079-4, 2001.

40   Parker, R.: The Rosemanowes HDR project 1983–1991, Geothermics, 28(4), 603–615, doi:10.1016/S0375-6505(99)00031-0, 1999.

Pearson, C.: The relationship between microseismicity and high pore pressures during hydraulic stimulation experiments in low permeability granitic rocks, Journal of Geophysical Research: Solid Earth, 86(B9), 7855–7864, doi:10.1029/JB086iB09p07855, 1981.

45   Preisig, G., Eberhardt, E., Gischig, V., Roche, V., Baan, M. van der, Valley, B., Kaiser, P. K., Duff, D. and Lowther, R.: Development of connected permeability in massive crystalline rocks through hydraulic fracture propagation and shearing accompanying fluid injection, Geofluids, 15(1–2), 321–337, doi:10.1111/gfl.12097, 2015.

Rahman, M. K., Hossain, M. M. and Rahman, S. S.: A shear-dilation-based model for evaluation of hydraulically stimulated naturally fractured reservoirs, International Journal for Numerical and Analytical Methods in Geomechanics, 26(5), 469–497, doi:10.1002/nag.208, 2002.

Rivet, D., De Barros, L., Guglielmi, Y., Cappa, F., Castilla, R. and Henry, P.: Seismic velocity changes associated with aseismic deformations of a fault stimulated by fluid injection, Geophysical Research Letters, 43(18), 9563–9572, doi:10.1002/2016GL070410, 2016.

Rummel, F. and Kappelmeyer, O.: The Falkenberg geothermal frac-project: concepts and experimental results. Hydraulic fracturing and geothermal energy. Springer, 1983.

Rutledge, J. T., Phillips, W. S. and Mayerhofer, M. J.: Faulting Induced by Forced Fluid Injection and Fluid Flow Forced by Faulting: An Interpretation of Hydraulic-Fracture Microseismicity, Carthage Cotton Valley Gas Field, Texas, Bulletin of the Seismological Society of America, 94(5), 1817–1830, doi:10.1785/012003257, 2004.

Rutqvist, J.: Determination of hydraulic normal stiffness of fractures in hard rock from well testing, International Journal of Rock Mechanics and Mining Sciences & Geomechanics Abstracts, 32(5), 513–523, doi:10.1016/0148-9062(95)00039-J, 1995.

Saar, M. O. and Manga, M.: Seismicity induced by seasonal groundwater recharge at Mt. Hood, Oregon, Earth and Planetary Science Letters, 214(3), 605–618, doi:10.1016/S0012-821X(03)00418-7, 2003.

Sasaki, S.: Characteristics of microseismic events induced during hydraulic fracturing experiments at the Hijiori hot dry rock geothermal energy site, Yamagata, Japan, Tectonophysics, 289(1), 171–188, doi:10.1016/S0040-1951(97)00314-4, 1998.

Schaltegger, U. and Corfu, F.: The age and source of late Hercynian magmatism in the central Alps: evidence from precise U−Pb ages and initial Hf isotopes, Contr. Mineral. and Petrol., 111(3), 329–344, doi:10.1007/BF00311195, 1992.

Schopper, F., Doetsch, J., Villiger, J., Krietsch, H., Gischig, V. S., Jalali, M. R., Amann, F., Dutler, N. and Maurer, H.: On the variability in pressure propagation during hydraulic stimulation based on seismic velocity observations, JGR: SolidEarth, under review.

Segall, P.: Earthquakes triggered by fluid extraction, Geology, 17(10), 942–946, doi:10.1130/0091-7613(1989)017<0942:ETBFE>2.3.CO;2, 1989.

Segall, P. and Fitzgerald, S. D.: A note on induced stress changes in hydrocarbon and geothermal reservoirs, Tectonophysics, 289(1), 117–128, doi:10.1016/S0040-1951(97)00311-9, 1998.

Shapiro, S. A., Huenges, E. and Borm, G.: Estimating the crust permeability from fluid-injection-induced seismic emission at the KTB site, Geophysical Journal International, 131(2), F15–F18, doi:10.1111/j.1365-246X.1997.tb01215.x, 1997.

Stein, R. S.: The role of stress transfer in earthquake occurrence, Nature, 402(6762), 605–609, doi:10.1038/45144, 1999.

Tester, J. W., Anderson, B. J., Batchelor, A., Blackwell, D., DiPippo, R., Drake, E., Garnish, J., Livesay, B., Moore, N., Nichols, K. and et al.: The future of geothermal energy., in Impact of Enhanced Geothermal Systems (EGS) on the United States in the 21st Century, vol. 372, Massachusetts Institute of Technology, Cambridge, MA., 2006.

Tomac, I. and Sauter, M.: A review on challenges in the assessment of geomechanical rock performance for deep geothermal reservoir development, Renewable and Sustainable Energy Reviews, 82, 3972–3980, doi:10.1016/j.rser.2017.10.076, 2018.

Townend, J. and Zoback, M. D.: How faulting keeps the crust strong, Geology, 28(5), 399–402, doi:10.1130/0091-7613(2000)28<399:HFKTCS>2.0.CO;2, 2000.

Tsang, Y. W.: The Effect of Tortuosity on Fluid Flow Through a Single Fracture, Water Resources Research, 20(9), 1209–1215, doi:10.1029/WR020i009p01209, 1984.

Villiger, L., Gischig, V. S., Doetsch, J., Krietsch, H., Dutler, N. O., Jalali, M., Valley, B., Selvadurai, P. A., Mignan, A., Plenkers, K., Giardini, D., Amann, F. and Wiemer, S.: Influence of reservoir geology on seismic response during decameter scale hydraulic stimulations in crystalline rock, Solid Earth Discussions, 1–46, doi:https://doi.org/10.5194/se-2019-159, 2019.

Vogler, D., Settgast, R. R., Annavarapu, C., Madonna, C., Bayer, P. and Amann, F.: Experiments and Simulations of Fully Hydro-Mechanically Coupled Response of Rough Fractures Exposed to High-Pressure Fluid Injection, Journal of Geophysical Research: Solid Earth, 123(2), 1186–1200, doi:10.1002/2017JB015057, 2018.

Wallroth, T., Eliasson, T., and Sundquist, U.: Hot dry rock research experiments at Fjällbacka, Sweden, Geothermics, *28*(4-5), 617-625, 1999.

Wehrens, P., Berger, A., Peters, M., Spillmann, T. and Herwegh, M.: Deformation at the frictional-viscous transition: Evidence
5   for cycles of fluid-assisted embrittlement and ductile deformation in the granitoid crust, Tectonophysics, 693, 66–84, doi:10.1016/j.tecto.2016.10.022, 2016.

Wenning, Q. C., Madonna, C., de Haller, A. and Burg, J.-P.: Permeability and seismic velocity anisotropy across a ductile–brittle fault zone in crystalline rock, Solid Earth, 17, 2018.

Zangerl, C., Evans, K. F., Eberhardt, E. and Loew, S.: Normal stiffness of fractures in granitic rock: A compilation of
10   laboratory and in-situ experiments, International Journal of Rock Mechanics and Mining Sciences, 45(8), 1500–1507, doi:10.1016/j.ijrmms.2008.02.001, 2008.

Zimmerman, R. and Main, I.: Hydromechanical Behavior of Fractured Rocks, in International Geophysics, vol. 89, pp. 363–421, Elsevier., 2004.

Zoback, M. D.: Reservoir Geomechanics, Cambridge Univ. Press., 2010.

15   Zoback, M. D. and Harjes, H.-P.: Injection-induced earthquakes and crustal stress at 9 km depth at the KTB deep drilling site, Germany, Journal of Geophysical Research: Solid Earth, 102(B8), 18477–18491, doi:10.1029/96JB02814, 1997.

APPENDIX
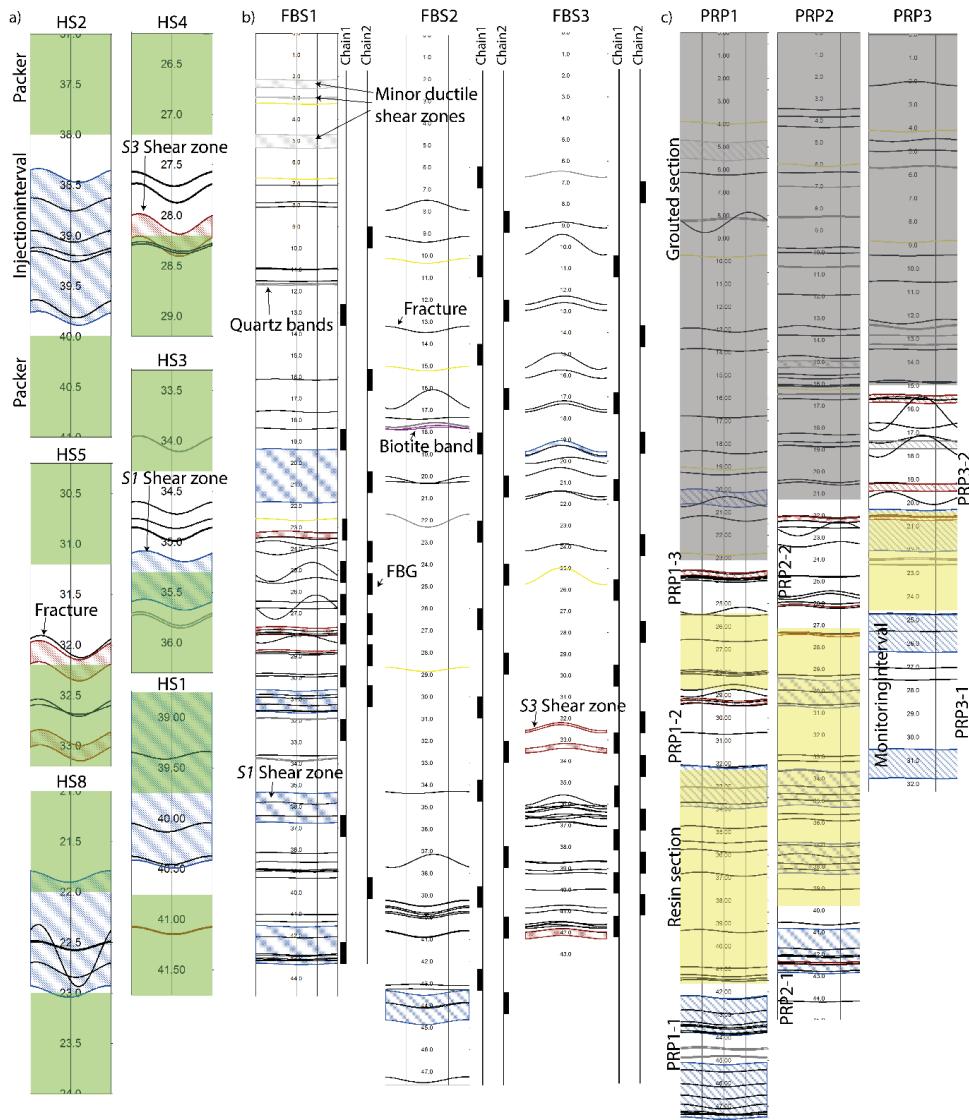
Figure A1. a) Structure logs of injection intervals, b) structure logs of strain monitoring boreholes with sensor locations, and c) customized packer system in the PRP boreholes, including open intervals, concrete and resin sections. Note that the actual packers
5 **surrounding the open intervals are not shown here, due to their length of only 20 cm.**
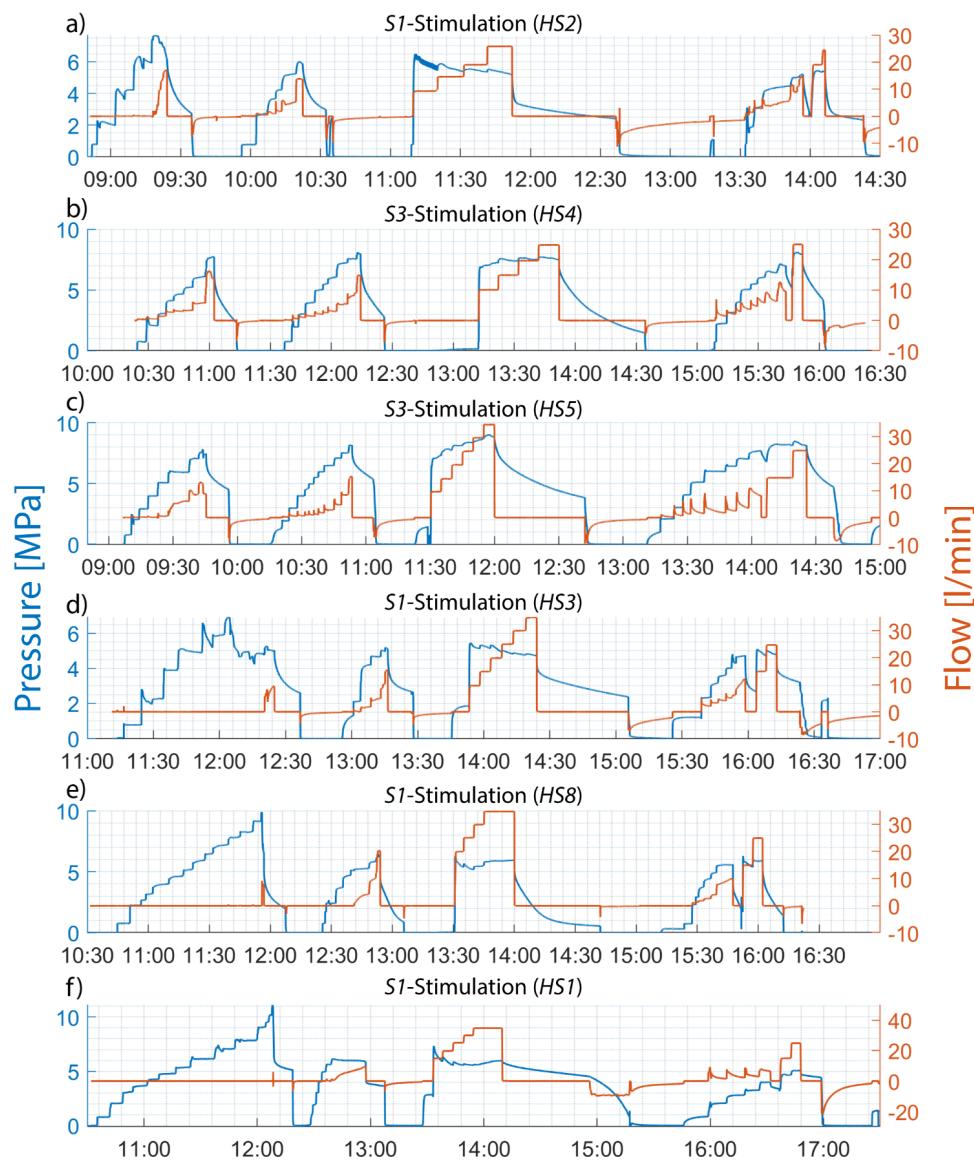
Figure A2. Injection protocols for all experiments. The tests are in chronological order.
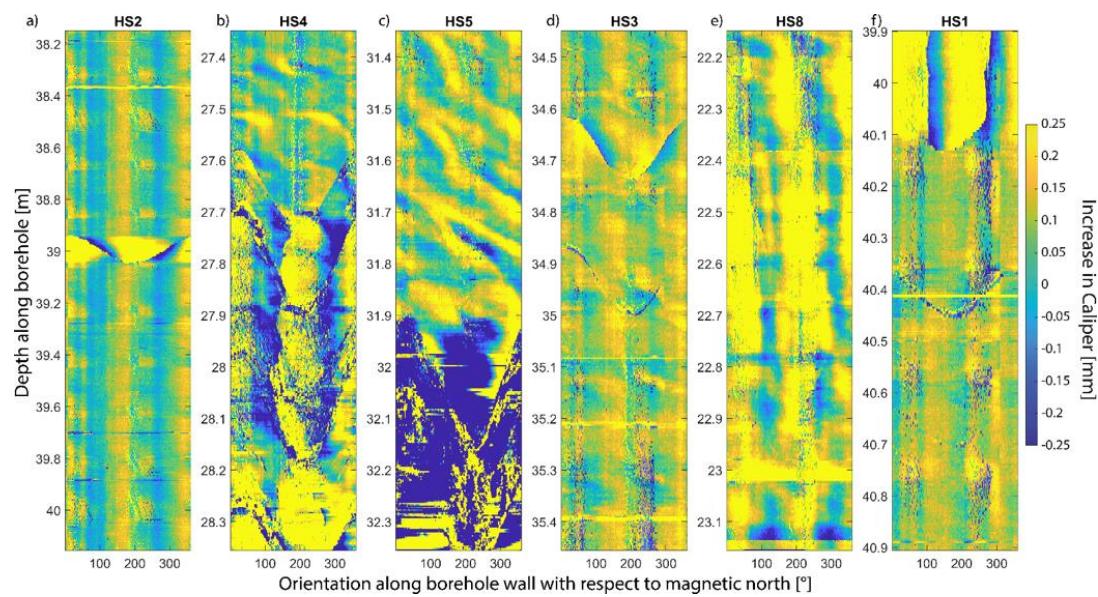
Figure A3. Difference plots from ATV logs. Logs are in chronological order.
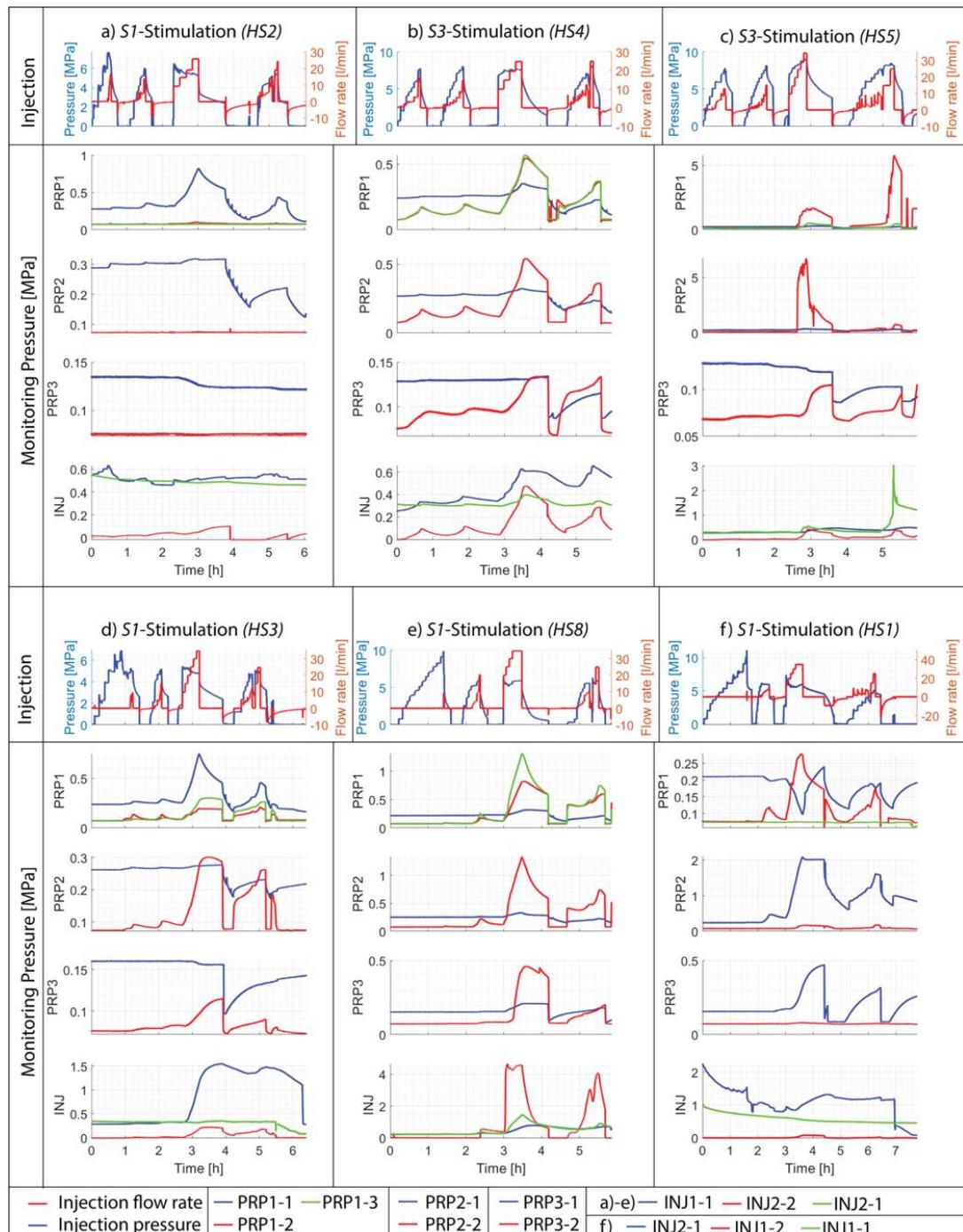
Figure A4. Pressure perturbation time series for all monitoring intervals. The shut-in moments are marked as vertical lines. Note that all intervals were vented after a period of shut-in.
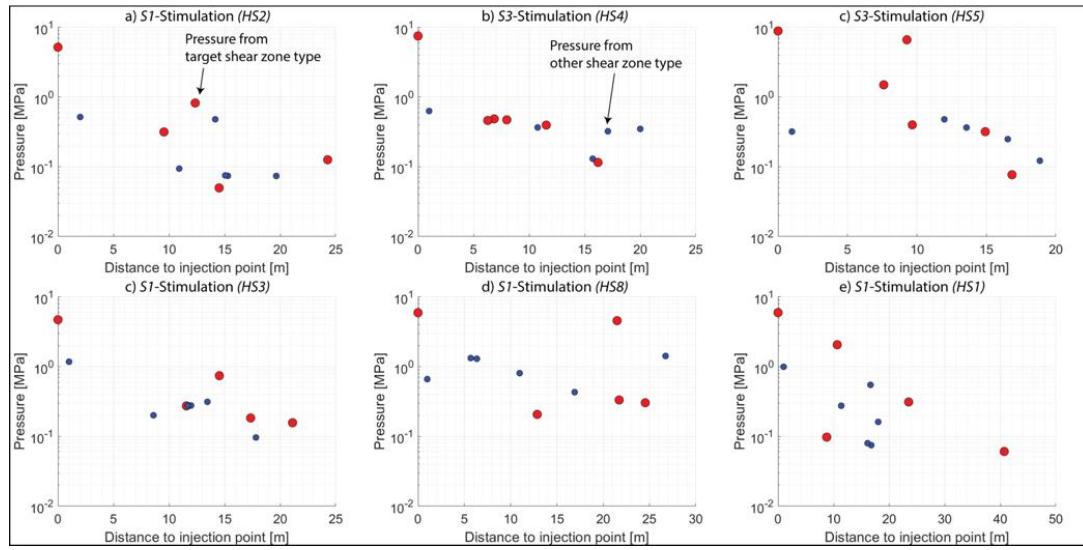
Figure A5. Pressure signals at the moment of shut-in after *C3* with respect to radial distance to injection point.
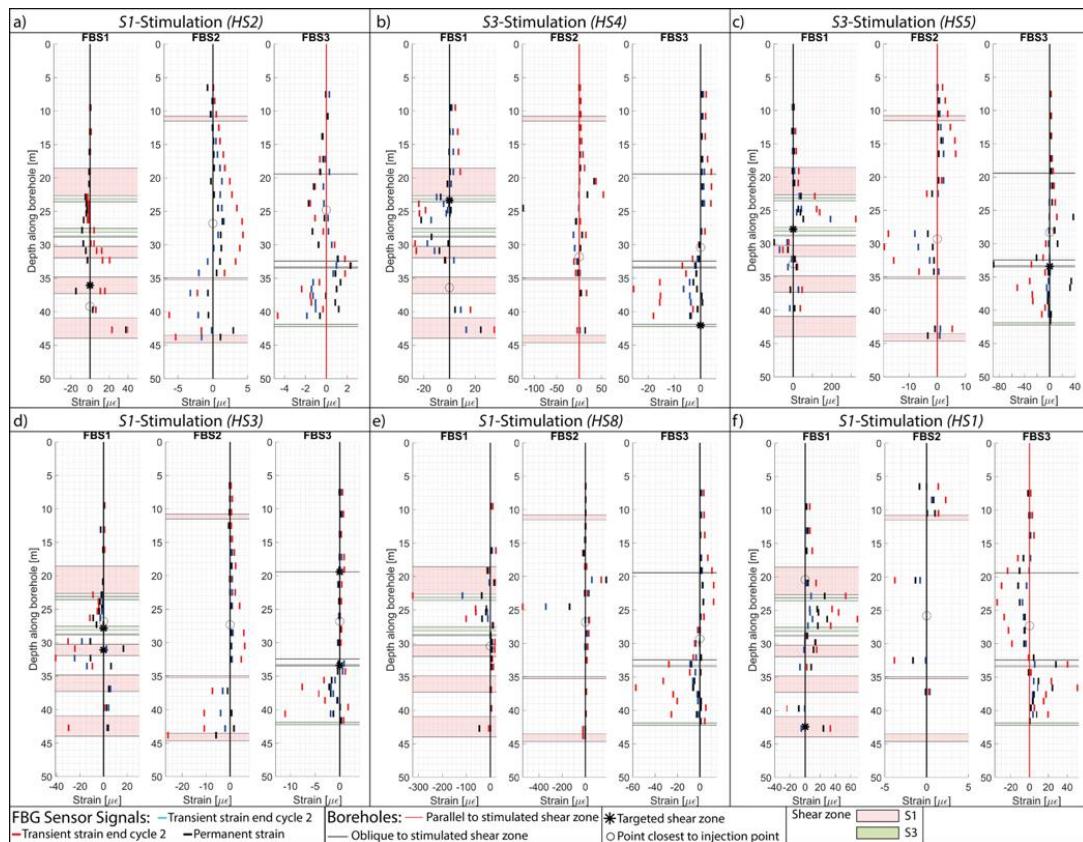
Figure A6. Strain along borehole axis picked transient at the end of injection cycle 2 and 3, and the permanent strain signal after the experiment.
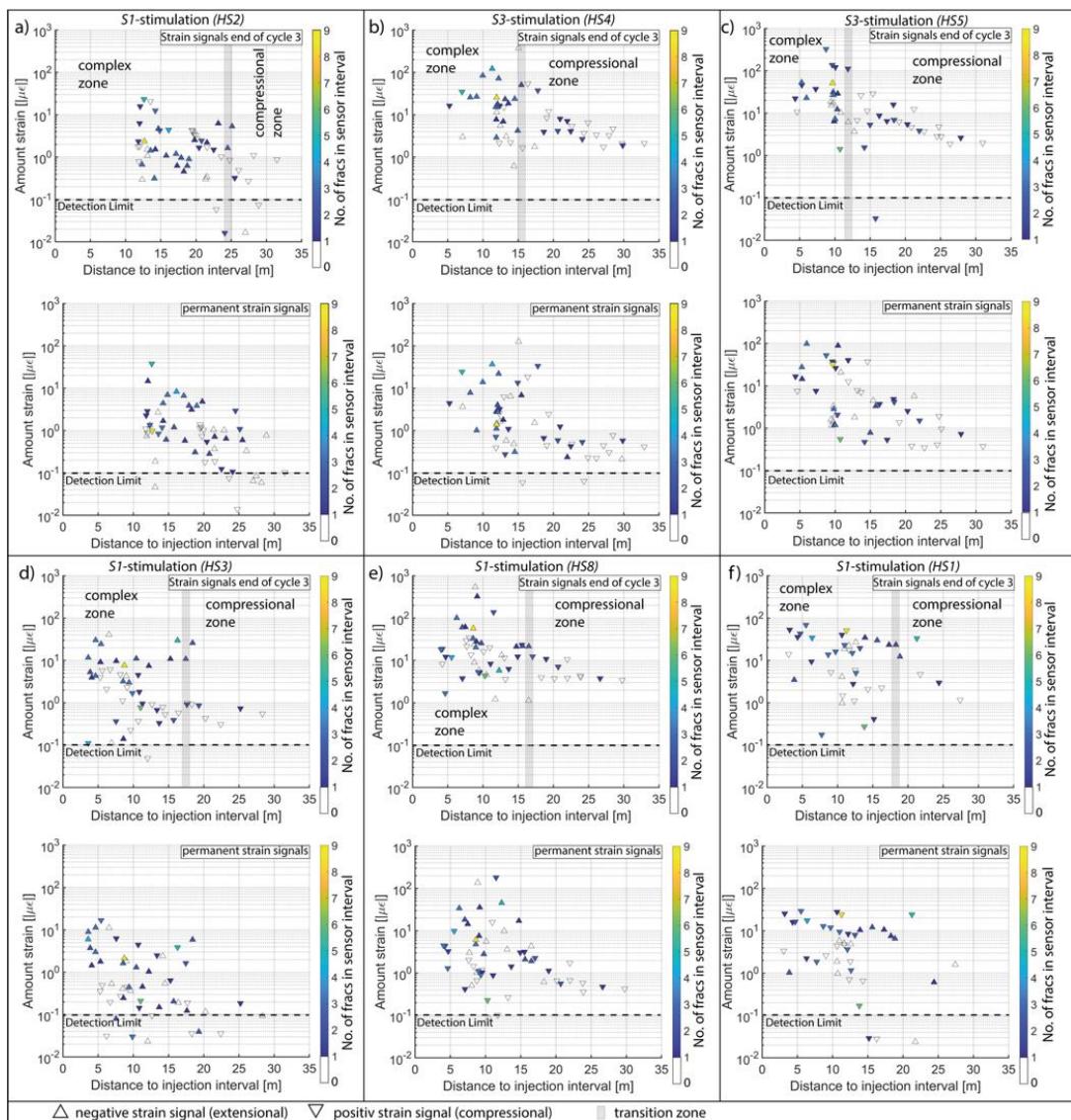
Figure A7 Strain signals with respect to distance to injection point for all experiments. The variable and compressional strain fields are labelled during *C3*.
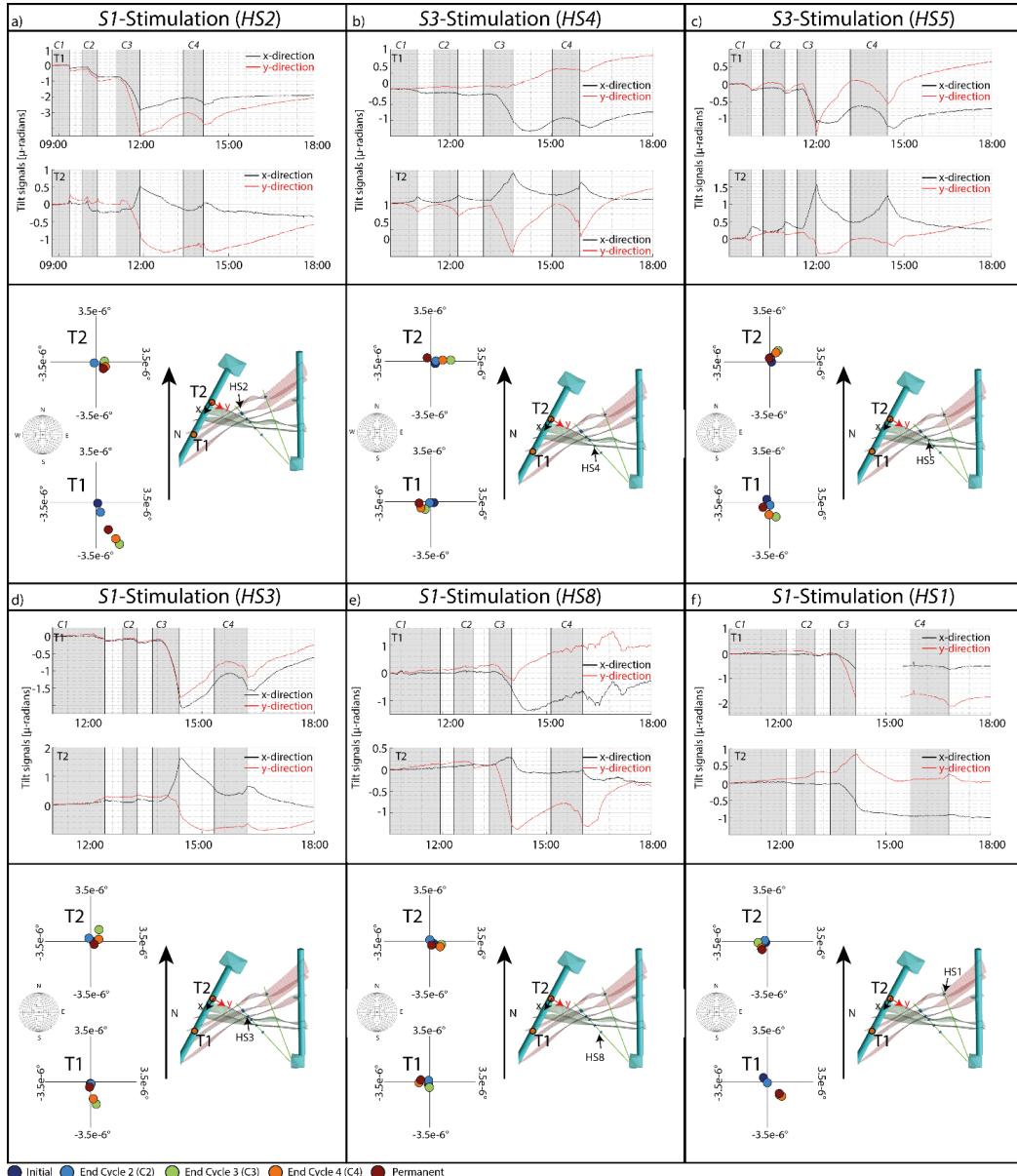
Figure A8. Inclinometer data for each of the six experiments. The upper panel shows the tilt time series for both experiments with the injection periods marked by the shaded vertical bands. The lower panel shows a horizontal section through the study volume at the level of the tunnels showing the shear-zones and tiltmeter T1 and T2 positions. The x- and y-axes of the tilt data are indicated on T2. Changes in the downward-oriented normal vector of the tunnel floor at T1 and T2 are shown in the lower-hemisphere plots at the left of the frames.

Table A1. Radial distances between the midpoints of the pressure monitoring intervals and the injection interval for all HS tests. The "OBS" intervals represent the inactive INJ borehole.

Interval	HS2	HS4	HS5	HS3	HS8	HS1
PRP1_1	11.9	19.6	16.4	14.2	24.1	15.2
PRP1_2	11.79	7.8	7.7	8.9	10.6	8.2
PRP1_3	16.3	7.1	9.9	12.5	6.2	11.2
PRP2_1	9.2	16.7	13.4	11.2	21.3	12.2
PRP2_2	16.0	6.6	9.4	12.1	5.5	10.8
PRP3_1	20.2	16.2	16.9	18.0	16.8	17.4
PRP3_2	25.0	16.0	18.9	21.4	13.1	20.2
OBS_2	14.7	10.7	13.1	15.4	11.8	16.0
OBS_1	15.3	15.7	14.3	14.0	15.0	18.1
INJ-1	4.0	9.4	7.4	5.9	12.0	9.5

Table A2. Response behavior of the pressure monitoring intervals at shut-in of injection cycle 3 for all HS tests. This table also makes the link to the shear zone targeted during each stimulation and covered by the monitoring intervals (both in bold). The responses are classified as immediate (in case of an immediate response to shut-in) and delayed (in case of a delayed response to shut-in). The underlined responses are from the intervals that covered the exact targeted shear zones. The ones in italic are taken from the intervals that do not cover the targeted shear zones.

	Stimulated shear zone type	S1	S3	S3	S1	S1	S1
Covered shear zone type	Interval	HS2	HS4	HS5	HS3	HS8	HS1
S1	PRP1-1	_immediate_	_immediate_	-	_immediate_	_delayed_	_immediate_
S3	PRP1-2	_immediate_	_delayed_	_delayed_	_immediate_	_immediate_	_immediate_
S3	PRP1-3	-	_delayed_	_delayed_	_delayed_	_immediate_	-
S1	PRP2-1	_immediate_	_immediate_	_immediate_	_immediate_	_immediate_	_immediate_
S3	PRP2-2	_immediate_	_delayed_	_delayed_	_delayed_	_immediate_	_immediate_
S1	PRP3-1	-	-	_immediate_	_immediate_	_immediate_	_delayed_
S3	PRP3-2	-	_delayed_	_delayed_	_delayed_	_delayed_	_immediate_
Depends on test	INJ2-2	_delayed_	_delayed_	_delayed_	_delayed_	_immediate_	
Depends on test	INJ2-1	-	_immediate_	_immediate_	-	_immediate_	-
Depends on test	INJ1-2	-	-	-	-	-	_delayed_
Depends on test	INJ1-1	-	_immediate_	_delayed_	_delayed_	_immediate_	-